8-2018

A STUDY OF THE EFFECTS AND SIGNIFICANCE OF TRANSITION MODELING FOR ROTORCRAFT APPLICATIONS

Ashwin Parwani
University of Tennessee, aparwani@vols.utk.edu

To the Graduate Council:

I am submitting herewith a thesis written by Ashwin Parwani entitled "A STUDY OF THE EFFECTS AND SIGNIFICANCE OF TRANSITION MODELING FOR ROTORCRAFT APPLICATIONS." I have examined the final electronic copy of this thesis for form and content and recommend that it be accepted in partial fulfillment of the requirements for the degree of Master of Science, with a major in Aerospace Engineering.

James G. Coder, Major Professor

We have read this thesis and recommend its acceptance:

Ryan S. Glasby, Stephanie C. TerMaath

Accepted for the Council:
<u>Dixie L. Thompson</u>

Vice Provost and Dean of the Graduate School

(Original signatures are on file with official student records.)

A STUDY OF THE EFFECTS AND SIGNIFICANCE OF TRANSITION MODELING FOR ROTORCRAFT APPLICATIONS

A Thesis Presented for the

Master of Science

Degree

The University of Tennessee, Knoxville

Ashwin Parwani

August 2018

ACKNOWLEDGEMENTS

ABSTRACT

A four-blade helicopter rotor is modeled using computational fluid dynamics (CFD), and the impact on the flow-field with and without a floating fuselage geometry is assessed. The numerical predictions were made with CFD simulations using the NASA OVERFLOW 2.2n solver. For numerical simulations, the flow-field was discretized in a structured, overset topology with grids intended to solve the scope of the problem. Results based on a tip Mach number of 0.58 were acquired for various collective pitch angles. The simulations were completed with the Spalart-Allmaras (SA) one equation eddy-viscosity turbulence model along with the Spalart-Shur rotation/curvature correction coupled with the amplification factor transport (AFT) transition model. Additionally, Delayed, Detached Eddy Simulation (DDES) was used to induce hybrid RANS/LES behavior. Overall predicted figure of merit and laminar-to-turbulent transition patterns on the blade surfaces with and without the fuselage exhibited reasonable agreement with experimental data. Specifically, laminar-turbulent transition patterns on the blade surfaces at 10° collective pitch showed better agreement with experimental data than at 8° collective pitch. It was observed from the simulations that the blade root and tip vortex systems become increasingly unstable as the collective pitch is increased for both configurations.

TABLE OF CONTENTS

LIST OF TABLES

LIST OF FIGURES

NOMENCLATURE

C_Q	=	rotor torque coefficient
C_T	=	rotor thrust coefficient
c	=	blade chord length
d	=	nearest wall distance
FOM	=	figure of merit
M_{tip}	=	rotor tip Mach number
N_b	=	number of blades
N_{crit}	=	critical amplification factor
$\tilde{n}$	=	approximate envelope amplification factor
P	=	pressure
R	=	rotor radius
Re	=	Reynolds number based on chord length
S_{ij}	=	mean strain-rate tensor
u, v, w	=	Cartesian velocity components
$\overline{u_i u_j}$	=	Reynolds stress tensor
x, y, z	=	Cartesian coordinates
γ	=	intermittency
μ	=	molecular viscosity
μ_t	=	turbulent eddy viscosity
ν	=	kinematic viscosity
$\tilde{\nu}$	=	modified eddy viscosity
Ω	=	vorticity magnitude
ρ	=	density
σ	=	rotor solidity
θ	=	rotor collective pitch

CHAPTER 1
INTRODUCTION

Design specifications for rotorcraft allow various abilities such as hover, forward-flight, and retreat [1]. Helicopters are unique due to their ability to hover and move backwards compared to fixed-wing aircraft. The first practical helicopter was the VS-300 designed by Igor Sikorsky in 1939 as shown in Figure 1.1 [1]. The design was able to perform simple maneuvers such as hover, fly backwards, and fly sideways, but the helicopter experienced issues with forward flight due to the downwash effects from the main rotor. This helicopter served as a stepping stone for future designs to come [1].
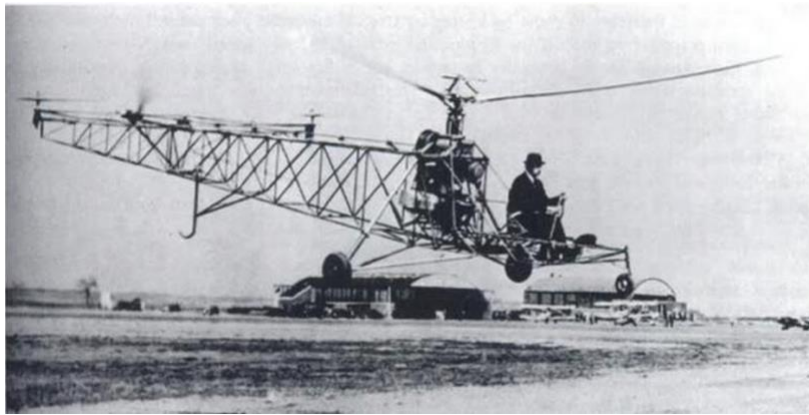
Figure 1.1 Sikorsky's VS-300 helicopter in flight (From Ref. [1]).

Many 4-bladed rotorcraft designs have been suggested to advance hover and cruise performance capabilities in terms of thrust and torque while enhancing overall efficiency. Modern helicopters from various manufactures such as Bell, Sikorsky (Lockheed-Martin), Airbus, Robinson, Boeing, and Leonardo have achieved capabilities allowing them to serve as rescue, military, and transport vehicles [1]. The Sikorsky UH-60 Black Hawk helicopter served mainly as the U.S. Army's tactical transport vehicle and has been used as a utility vehicle in internationally as well [2, 3]. It was designed with twin engines and four main

rotor and tail blades as shown in Figure 1.2. The Black Hawk's roles as a utility vehicle include medical evacuation, special operations, and aerial firefighting as well as multiple others [4].

Figure 1.2 Sikorsky's UH-60M Black Hawk helicopter in flight (From Ref. [4]).

Another internationally recognized utility helicopter was the Bell 412. This four-bladed helicopter was designed by modifying the two-bladed Bell 212. The vehicle was initially used for military and medical purposes but has also become a commercial vehicle. Additionally, the helicopter is used in law enforcement and for transporting fuels and gases [5, 6].

Unlike the previous helicopters discussed, the Boeing AH-64 Apache was developed as a U.S. attack helicopter as shown in Figure 1.3. The model was originally designed based on the Model 77 by Hughes Helicopters which was selected over the Bell YAH-63 by the U.S. Department of Defense. The design was selected for its advanced maneuvering capabilities and powerful engine. The helicopter also featured 4 blades for the tail and main rotors [7, 8].

Figure 1.3 Boeing's AH-64 Apache (From Ref. [8]).

As helicopter designs continued to advance, the Northrop Grumman MQ-8 Fire Scout was developed as one of the earlier unmanned autonomous helicopters made as shown in Figure 1.4. The MQ-8 design was based on the RQ-8 model which was the first unmanned helicopter to land on a mobile U.S. Naval ship. The MQ-8 was designed with four blades compared to the three-bladed RQ-8. The helicopter was developed as a scouting vehicle and as aerial support for air, ground, and sea military forces [9, 10].

Figure 1.4 Northrop Grumman MQ-8 Fire Scout (From Ref. [10]).

As rotorcraft developments continue to be made, hover is an essential consideration when designing rotorcraft because this condition can both constrain the vehicle's capabilities and influence the power requirements. The process of numerically modeling rotorcraft in hover configurations accurately remains a challenge due to the discretization resolution requirements because of the flow field complexity [11-14]. With respect to flow-field complexity, the vorticity generated by the tip creates a strong helical structure beneath the rotor through self-induction. Accurate numerical modeling of this vortex system is essential for predicting performance characteristics, but the wake is difficult to model due to flow instabilities [11-14].

Computational fluid dynamics (CFD) modeling presents an innovative approach to determine dominant flow characteristics that are essential in predicting flow. Recent developments in prediction methods have shown significant impacts on accuracy for performance computations [14]. Simulations assuming fully turbulent flow of a rotor in hover have been widely utilized [15-26], but they do not completely capture the flow physics of a rotor in hover [14]. The development of transition modeling [27-31] in conjunction with established turbulence models [32-37] is ongoing. This technology has been applied to predict a rotor in hover [38-47].

Transition modeling in rotorcraft simulations has provided a significant challenge and is of current community interest [48]. Transitional flow is heavily present in low Reynolds number computations which makes understanding transition relevant when predicting performance parameters [48]. Experimental data from wind tunnel testing has allowed validation for CFD solutions to assess the accuracy and capabilities of various fully turbulent and transition models [49-51]. Solutions obtained from the proposed work will test the current transition model abilities and provide feedback to possible changes to enhance predictive capability.

1.1 Goals and Research Approach

The goal of the current work is to determine the effects of transition modeling and its significance for rotorcraft applications. Additionally, the studies are conducted to

explore the simulation capabilities of a recently developed CFD-based transition model. Challenges with transition modeling include accuracy and expense based on grid generation techniques and solution schemes. The current study explores the predictive capabilities of the computational scheme used and assesses the accuracy compared to measurements made by Overmeyer and Martin [51]. The study covers grid generation methods used and convergence history utilizing a transition model for a Pressure Sensitive Paint (PSP) rotor [52] in hover. The capabilities of the CFD approach with a transition model to accurately model a complex flow-field is tested by simulating rotor-fuselage interactions using a PSP rotor and a NASA Rotor Body Interaction (ROBIN) [53] fuselage. The impact of including the fuselage in conjunction with the rotor is assessed as well as comparisons made to experimental data.

CHAPTER 2
BACKGROUND

Aircraft designs are continuously updated to improve efficiency and performance [14]. Specifically, for rotorcraft, design variations are constantly suggested, such as varying rotor tip and hub shapes [14]. These design changes may significantly affect hover conditions for rotorcraft, and design alterations require accurate modeling, simulation, and testing to validate their performance benefits. CFD simulations [15-26, 38-47] have been beneficial to accurately generate hover predictions, and wind tunnel hover tests have allowed validation of CFD modeling capabilities [49-51]. Both CFD and experimental data generation have made numerous advancements through the years which will be discussed in this chapter.

One of the earliest methods for determining performance predictions of aerodynamic designs that is still used is Glauert's blade element momentum (BEM) theory [54]. The theory requires two-dimensional airfoil data to determine lift and drag forces and is based on one-dimensional momentum theory. Tabulated airfoil characteristics are used to determine the angle of attack, and the performance parameters are based on the Reynolds number, angle of attack, and airfoil characteristics. The concern with this method is the availability of airfoil data. It is difficult to determine predictions for design in which airfoil data is unavailable. These concerns motivated advancements in prediction methods for aerodynamic modeling [55].

Rotors were initially modeled around the 1970s based on Prandtl's lifting line theory. Each blade was modeled as a "lifting line" vortex, and the wake structure produced by the blades was represented by a deformed helix. Models were considered visualizing the displacement between the blades and tip vortices. Additionally, wake models were proposed based on capturing the velocity generated through blade vorticity. The various proposed wake models utilized were functional, but flaws including airfoil data requirements and minimal geometric variation were noticed for both proposed methods.

Modeling continued to expand to free wake evaluation using numerical integration and other methodology for forward flight which allowed a practical tip vortex system estimation [14].

Steady potential flow solvers for rotors were developed from available isolated wing models which eventually led to unsteady rotor solvers. The significant effects characterized by the vortex system were modeled using free or proposed wake models. The newer developments allowed visualization and analysis of some shocks and influence due to viscosity. Euler approaches advanced by solving the conservation equations with time dependent finite schemes which allowed hover calculations to seem more achievable [14].

With potential flow and Euler approximations advancing rotorcraft modeling up until the late 1980s, the next major improvement involved integrating Reynolds averaged Navier-Stokes (RANS) methods into flow solvers. The developed solvers allowed expansions in all areas of transonic flow rotor calculations, but they were costly and required external wake models similar to earlier developed solvers. In efforts to reduce computational time, domains were separated into a far-field region solved with the full potential equation and a near-body wake solved through Navier-Stokes equations. Additionally, high order methods became favorable to capture flow physics for rotors. Overset topology was utilized to enhance and resolve grid placement. The structured-grid surface patches provide an easier way to move a specific grid relative to others. Overset grid methods also introduced Cartesian grids to adequately model a vortex system, and to further advance grid generation efficiency, adaptive mesh refinement (AMR) was incorporated in numerous techniques [14].

Steady-state AMR was first employed by generating an initial solution and adapting the grid to extend the results based on a refined mesh. The methodology was advanced to unsteady AMR to account for more complex cases including rotor-body interactions. HELIOS [56] provides a computational approach generating a near-body solution using an unstructured mesh, and the off-body was created as a Cartesian mesh. This program advanced vertical flight computational techniques and allowed complex wake visualizations and predictions [14].

2.1 Fundamental Principles for Rotorcraft Modeling

To adequately model a rotor in hover, there are many factors to consider. The first factor to consider is grid generation. Overset grid schemes have been utilized for more than 30 years due to their various benefits [57-61]. Overset grids are developed by creating multiple overlapping grids around a geometry for domain discretization. They are beneficial in creating grids for complex geometries that require precise boundary representations or moving grids. Combined solutions are determined for the overlapping grids through interpolation at specific points. Points that are outside or inside the boundary of a specific grid are removed from computations defined as holes. Orphan points can exist in faulty overset grids due to lack of required overlap or insufficient information from the donor point. This refers to absent grid point boundary values required for interpolation [59]. Cartesian meshes are commonly used for off-body grid generation due to the complex aerodynamic interactions that occur in the flow-field suggesting uniform refinement. The meshes can be unstructured or block-structured which both adjust to the near-body grid used. Meakin et al. discusses typical minimum off-body grid spacing requirements for inviscid, viscous, and transitional simulations [58].

Another factor that essential to modeling a rotor in hover is the applied turbulence closure method. The two fundamental turbulence modeling strategies used are the Spalart-Allmaras (SA) one-equation eddy-viscoity turbulence model [32] and Menter's Shear Stress Transport (SST) two-equation turbulence model [33]. These models are integrable through the viscous sublayer and provide consistent predictions in which free-stream turbulence sensitivity is reduced. Models that look specifically at the boundary layer or algebraic models fail at conditions where flow separation occurs. The models also gave a more accurate application for unstructured modeling approaches and considered viscous effects in flows [32].

Another development in turbulence modeling strategies is the introduction of Detached Eddy Simulation (DES) [62] or Delayed, Detached Eddy Simulation (DDES) [63] as a hybrid Reynolds averaged Navier-Stokes–large-eddy simulations (RANS/LES) methodology. DES-type methods are intended to solve for attached boundary layers using

RANS modeling and switch to an LES-like behavior in separated regions. It is efficient for thin boundary layers where the wall spacing is set to its maximum and where the wall spacing is set to minimum values. At minimum wall spacings, RANS behavior is forced near the wall and a sub-grid scale methodology is used for a majority of the boundary layer. The region in between is modeled through LES behavior on the wall. Problems arise when the LES branch of DES becomes active in a boundary layer where there is insufficient grid resolution for LES. This leads to modeled stress depletion, which can contribute to premature separation of the flow. DDES provides a shielding function that tries to preserve the RANS behavior in attached boundary layers, irrespective of grid resolution. [63].

When simulating a rotor in hover, another essential consideration is effectively accounting for rotation and curvature effects [64]. Basic turbulence models have difficulties capturing the changes in turbulent shear flow predictions. Turbulence models based on Reynolds-stress terms are developed to account for rotation and curvature effects, but the computational costs are extensive. Additionally, accuracy is not completely promised with these methods. Applying the Spalart-Shur rotation/curvature correction suppresses turbulence production in vortex cores. Second derivatives of multiple velocity fields are used; however, the second derivatives make the approach more expensive and more prone to numerical errors. [64]. The approach is Galilean invariant and combines system effects caused by rotation and curvature [64].

2.2 Recent Fully Turbulent and Transition Simulations

Numerous efforts have been placed towards testing new advances in rotor simulation capabilities, including turbulence and transition modeling. The different research groups around the world working in this area tend to focus on specific subsets of simulation methods, but all are working towards improving the state of the art. [15-26, 38-47]. Research efforts at the Georgia Institute of Technology (Georgia Tech) have included overset grid adaption, rotor hover performance for assumed fully turbulent flows, and transition predictions for various geometries [15, 16, 38]. A new grid adaption strategy was presented by Shenoy, Smith, and Park to include grid adaption on the overset grids [15].

The method was based on the presence of vorticity around near-body grids, whereas previous grid adaption methods were used exclusively for off-body meshes. It was shown that the strategy was able to present new features in the simulations for rotor-fuselage interactions. A hybrid approach to predicting a rotor in hover with varying blade tip configurations using CFD along with a free-wake solver was discussed by Smith et al. [16]. Free-wake methods present a way to capture wake structures with greatly reduced cost requirements. However, these methods may not completely capture flow features in the entirety. The simulations were completed with the NASA OVERFLOW compressible flow solver [65] coupled with Continuum Dynamics Inc's free-wake solver, CHARM [66]. The hybrid strategy was able to maintain satisfactory results while significantly reducing computational time. An additional hybrid RANS/LES strategy including transition modeling was assessed by Hodara and Smith for various geometries [38]. The proposed method differed from traditional DDES approaches [63]. To allow for a smoother transition from RANS to LES behavior, a turbulent oscillation was added to the transition region to enhance the LES behavior. This approach allows predictions for flows that are largely separated.

Various fully turbulent simulations have been also completed by the University of Maryland [17-19]. CFD simulations using compressible flow solver, OVERTURNS [67], were completed by Baeder, Medida, and Kalra to compare thrust and torque predictions to experimental data [17]. Tip vortex features were also explored, and it was shown that the tip vortices maintain stability for the first few revolutions well. However, the root vortex was shown to expand in the first few revolutions. Additionally, unsteady fully turbulent simulations were completed by Jung, Govindarajan, and Baeder by applying a mixture of mesh systems [18]. Unstructured overset near-body grids using a Hamiltonian strand method were combined with a structured Cartesian background mesh. The method presented was able to extend to unsteady flows while maintaining fair convergence. To increase the accuracy of predictions, wake preservation was explored by Kalra and Baeder [19]. The predictions were able to show that assumed fully laminar flows portray a cleaner wake proving that increasing turbulence levels affects the quality of the wake. A higher

quality wake was observed by adding a modification for anisotropic meshes along with using DDES [63].

Out of the University of Liverpool and the University of Glasgow, simulations were performed by Garcia and Barakos [20, 39] utilizing the Helicopter Multi-Block CFD solver (HMB2) [68-70]. Fully turbulent and transition cases were simulated using different tip configurations as previously described [39]. It was shown that predictions agreed with measurements in terms of aerodynamic loads for all tip configurations. Full and model-scale hover performance predictions were obtained [20] with the HMB2 solver for varying collective pitch angles. It was analyzed that rotor configurations with anhedral predicted slightly higher figure of merit computations and a notable reduction in noise. Additional transition modeling simulations were applied for the XV-15 rotor by Garcia, Colonia, and Barakos [40] utilizing the HMB2 solver. These simulations showed significant increases in figure of merit. Differences in surface skin friction patterns were also noticed due to transition modeling. A grid refinement study was also completed by analyzing various grid resolutions along with three experimental data sets as shown in Figure 2.1.
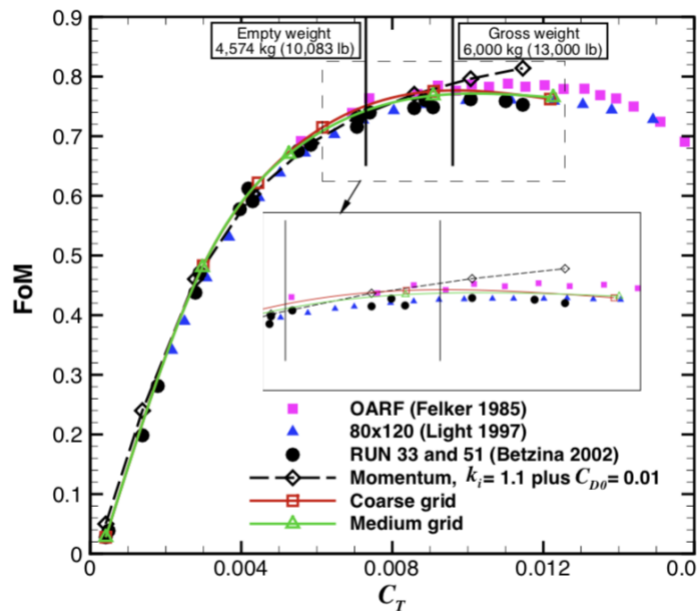
Figure 2.1 Grid refinement assessment based on hover performance (From Ref. [40]).

Fully turbulent and transition simulations with the Sikorsky S-76 rotor at the University of Toledo were completed by Sheng, Zhao, and Wang [41, 42] using the U²NCLE [71] solver. Hover performance effects due to varying turbulence models [41] were explored by comparing predictions with a combination of DDES [63], Langtry and Menter's local-correlation transition model [30], and a stall delay model (SDM). Results obtained with SDM matched well with provided experimental data and produced the highest figure of merit values. Similar simulations were conducted with three different blade tip configurations: tapered and swept, straight, and tapered and swept with anhedral [42]. The straight tip predictions were within 1% of experimental data in terms of figure of merit. Tip vortex patterns were also studied for the three configurations, and the paths diverged within the first revolution for each simulation. Additionally, fully turbulent and transitional hover simulations for the XV-15 were completed by Sheng, Zhao, and Hill [43] using the U²NCLE and HELIOS codes. For these simulations, the one-equation turbulence model [32] was utilized with both codes, and the local-correlation transition model was implemented through U²NCLE. Figure 2.2 displays performance predictions obtained along with experimental results. The models were able to predict thrust and torque values that compared well with available experimental data.
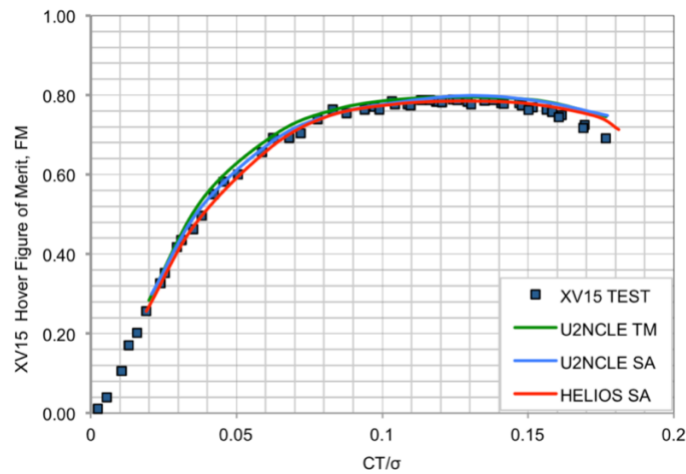
Figure 2.2 Measured and predicted XV-15 hover performance comparison using U²NCLE and HELIOS (From Ref. [43]).

12

Vieira, Kinzel, and Maughmer from Pennsylvania State University were able to complete fully turbulent and transition simulations using a model-scale PSP rotor in hover [47]. Transition modeling figure of merit predictions were fairly close to obtained experimental data, and the solutions showed improvement with a slightly finer mesh. Stability in the tip vortex system was enhanced, as shown in Figure 2.3, whereas previous attempts display noticeable instability. Additionally, the predicted transition locations matched up well measured transition locations, but further exploration is required for blade tip transition.
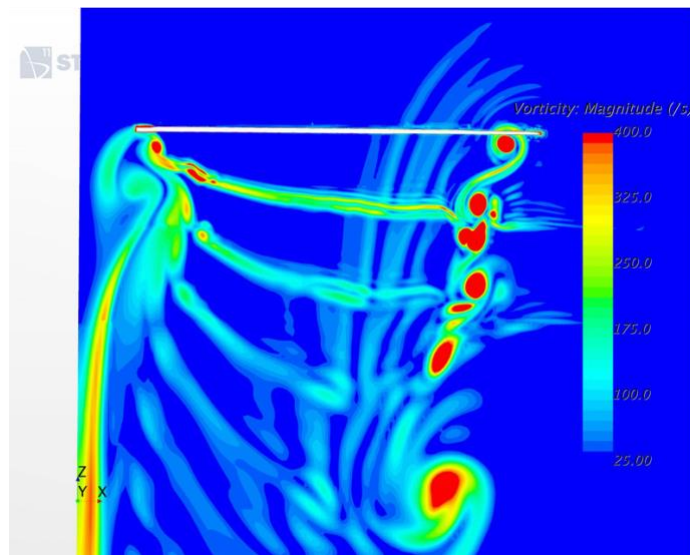
Figure 2.3 Vorticity magnitude highlighting tip vortex stability (From Ref. [47]).

Out of the NASA Ames Research Center, XV-15 fully turbulent simulations were studied by Yoon, Pulliam, and Chaderjian [21] to compare effects from using various turbulence models, grid resolutions, and other contributing factors. Simulations were completed for three grid resolutions ranging from coarse to fine meshes. The two turbulence models used were the SA one-equation turbulence model [32] with DES [62] and DDES [63] and Menter's SST two-equation turbulence model [33] with DDES. Figure 2.4 depicts the difference in figure of merit for the three grid resolutions. The fine grid was able to achieve a figure of merit prediction closer to experimental data than the coarse grid

by roughly 1%. The SST turbulence model was also able to provide more accurate predictions compared to the one-equation turbulence model. Yoon et al. continued turbulence modeling efforts on the XV-15 [22] by comparing the different approaches to solve the off-body grids. The SA one-equation turbulence model was utilized for near-body solutions, but in addition to the RANS-based off-body solver, the Laminar Off-Body (LOB) approach was compared to assess differences in wake behavior.
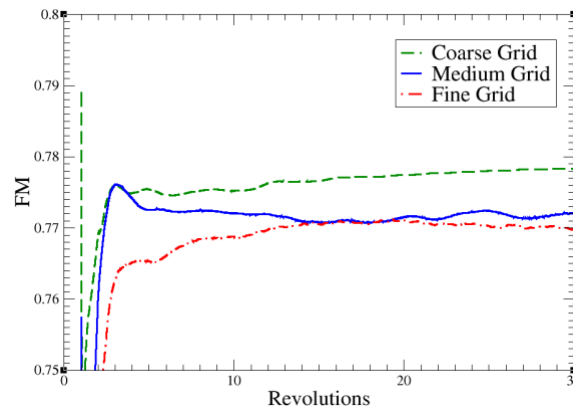
Figure 2.4 Grid resolution comparison (From Ref. [21]).

Studies with the S-76 were completed at NAVAIR and HPCMP CREATE-AV by Abras and Hariharan [25, 26] utilizing HELIOS with FUN3D [72] and kCFD near-body solvers. Grid refinement was analyzed to assess numerical accuracy [25]. The blade meshes were shown to require finer resolutions near the tip, trailing edge, and leading edge for accurate predictions. Using a coarse off-body mesh also had a negative impact on results because the vortex system was not completely captured. Tip shape variations were explored also with the kCFD near-body solver in Kestrel [26]. Predictions made with Kestrel were shown to capture the root vortex system as shown in Figure 2.5, however predictions made with HELIOS did not fully retain the root vortex. Additionally, it was noted that predictions with an anhedral blade tip produced greater hover performance accuracy similar to earlier mentions efforts.
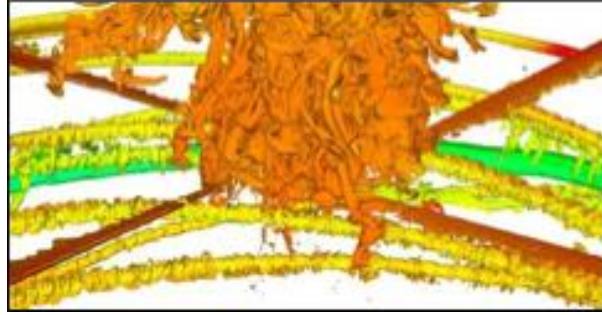
Figure 2.5 Root vortex system generated using Kestrel (From Ref. [26]).

Various fully turbulent and transitional hover predictions have also been completed by the U.S. Army Aviation Development Directorate [23, 24, 44-46]. S-76 fully turbulent simulations were completed by Jain and Potsdam [44] using the HELIOS solver [56] for two different tip Mach numbers. The near-body solver used was OVERFLOW [65], and the off-body solver was SAMARC. Similar to simulations out of the University of Toledo, tip vortex patterns and hover performance were analyzed in comparison with experimental measurements. Hover performance predictions using the solver combination showed slight underpredictions in figure of merit.

Simulation efforts were continued by Jain [45, 23] to further analyze modeling options and performance variation factors. Tip shape variation simulations [45] were completed using configurations described above [42] with the addition of a hub center body. It was noticed that the hover performance results were not significantly affected with the inclusion of a hub as seen in Figure 2.6 for the swept tapered tip configuration.
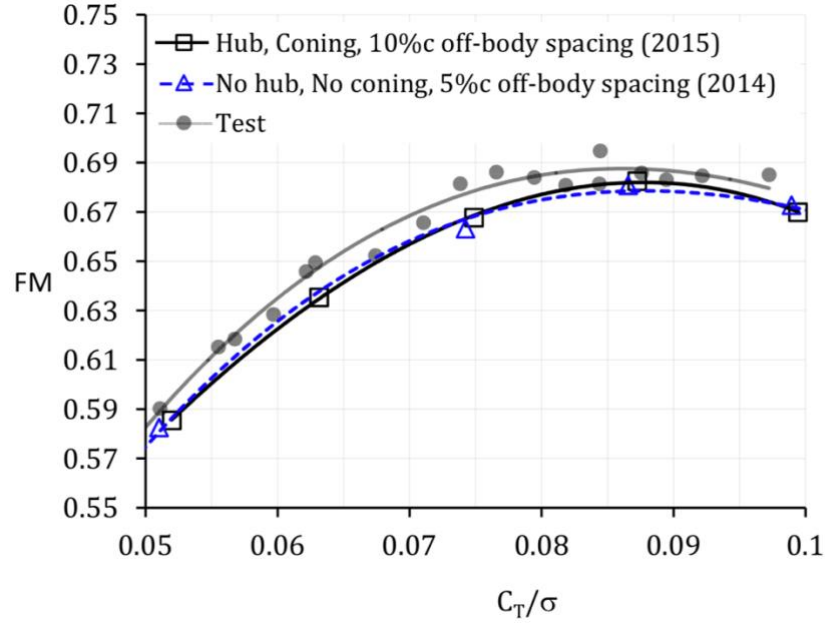
Figure 2.6 Hover performance setup comparison (From Ref. [45]).

It was also noted that a 5% chord spacing in the wake mesh was able to capture the tip vortex behavior significantly greater than a 10% chord spacing. However, determining tip vortex predictions was a difficult task due to the unstable behavior upon completing a full revolution. Various modeling approaches such as utilizing structured and unstructured meshes with various solver combinations were explored [23]. HELIOS was used for structured simulations with the OVERFLOW near-body solver and unstructured simulations with the FUN3D [72] near-body solver. The highest and most accurate to experimental data figure of merit predictions were achieved using unstructured meshes in HELIOS along with FUN3D. The wake structures were clearly defined but seemed to become unstable before completing a full revolution as expected. Figure 2.7 displays the rotor wake obtained through the OVERFLOW solver.

16
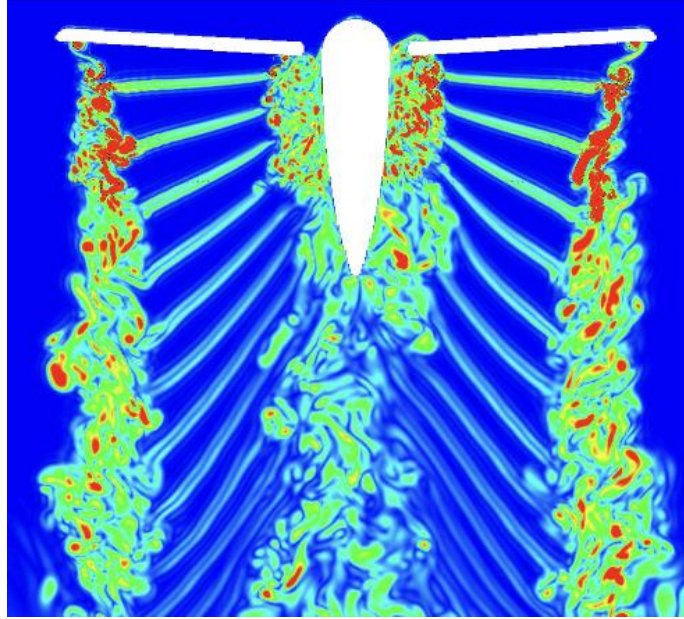
Figure 2.7 Vorticity magnitude contours for wake visualization (From Ref. [23]).

A particular study by Jain that inspired the current simulations analyzed hover performance for an isolated PSP rotor and an installed rotor with a ROBIN fuselage [46]. Both transition and fully turbulent cases were simulated at a tip Mach number of 0.58. Simulations were carried out utilizing HELIOS along with OVERFLOW and FUN3D for the near-body solutions. Simulations using OVERFLOW alone were also conducted for comparison. For turbulence closure, the Menter Shear Stress Transport (SST) k-ω model [34] was used along with the Langtry-Menter γ-$\tilde{R}e_{\theta t}$ transition model [30]. To aid with excess turbulence visualization in the core vortex system, a curvature correction [64] was added. Additionally, for the simulations with OVERFLOW alone, the turbulence model was coupled with DES to improve wake behavior. Unstructured, overset grid systems were generated for the blades and the fuselage, but the blades were also generated using a structured, overset grid. The unstructured fuselage grid was created using isotropic triangular cells as shown in Figure 2.8.
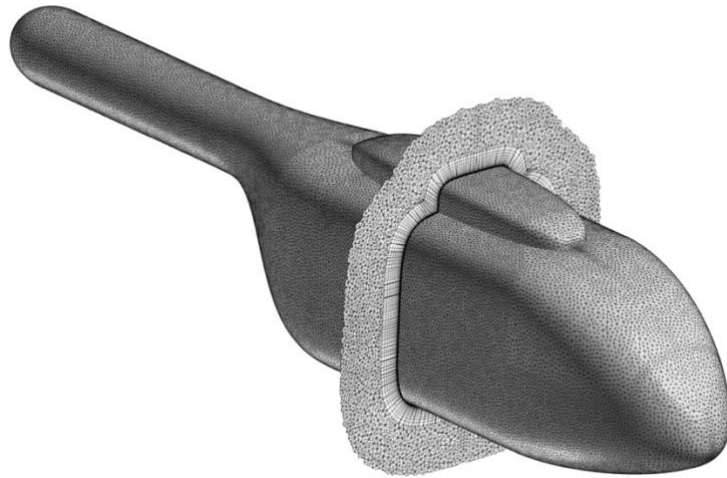
Figure 2.8 ROBIN fuselage unstructured, overset grid (From Ref. [46]).

Fully turbulent and transition cases were simulated at collective pitch angles of 6°, 8°, 10°, and 11°. The hover performance for the installed rotor transition cases were shown to match well with experimental data, especially for high thrust data. Slight discrepancies were noticed possibly due to testing facility effects or possible uncertainties within the experimental data. As expected, installed rotor figure of merit values were greater than isolated rotor values due to up-wash effects caused by the fuselage as shown in Figure 2.9. It is essential to improve modeling methods to reduce the differences between data sets even further [46].
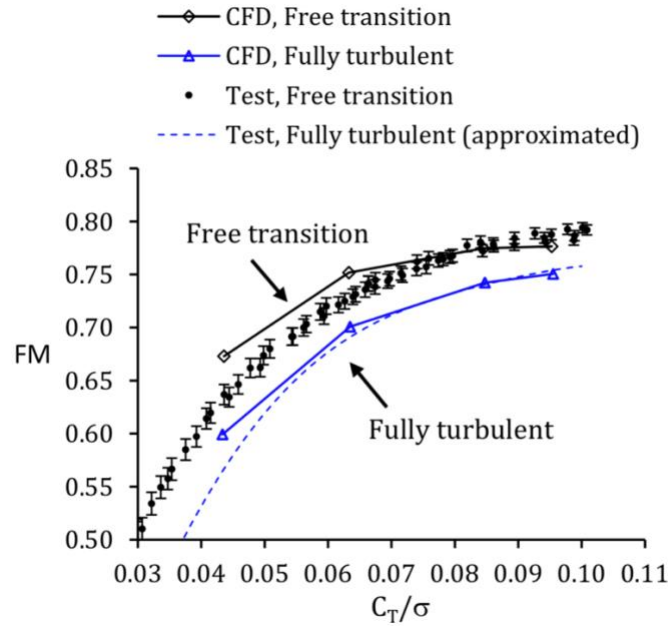
Figure 2.9 Installed and isolated rotor performance comparison to experimental data (From Ref. [46]).

Transition locations and wake structures were also examined. A trip in the flow due to higher thrust experienced by blades directly above the fuselage was noticed. Higher thrust was caused by fuselage up-wash effects or reduction in downwash. The blades that were not directly above the fuselage during the current revolution displayed transition patterns similar to an isolated rotor case. Both installed rotor and isolated rotor wake structures presented similar behavioral patterns, but differences were noticed due to fuselage effects including increased up-wash near the hub and tip vortex instabilities near the fuselage tail. Also, the tip vortex system seemed to become more unstable as the wake structure grew with additional revolutions as expected. Figure 2.10 shows the computed wake structure for the installed rotor case [46]. Facility effects on hover performance were explored by Jain [24] through CFD computations. In addition to the PSP rotor, a representation of the test stand was developed for the future simulations with the HVAB rotor blades as shown in Figure 2.11. Multiple configurations were considered with the test stand by adjusting heights for the ground and ceiling planes, however, effects due to tunnel installation placed minimal effect on hover performance factors.
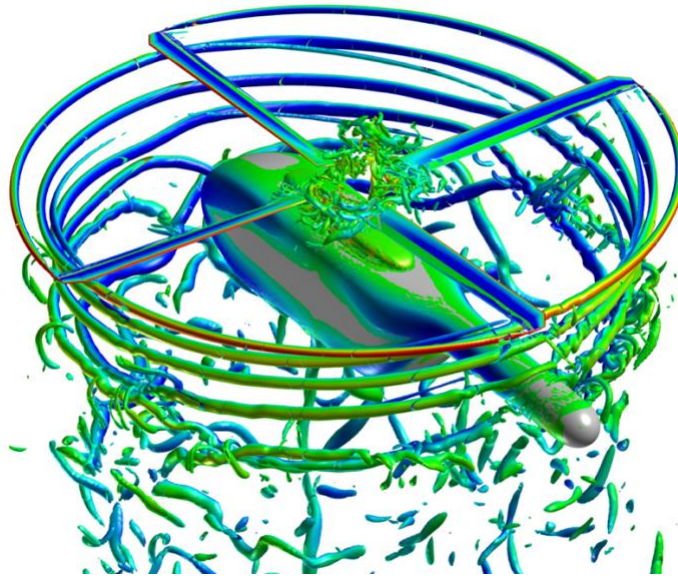
Figure 2.10 Iso-surfaces of Q-Criterion = 0.001 (From Ref. [46]).
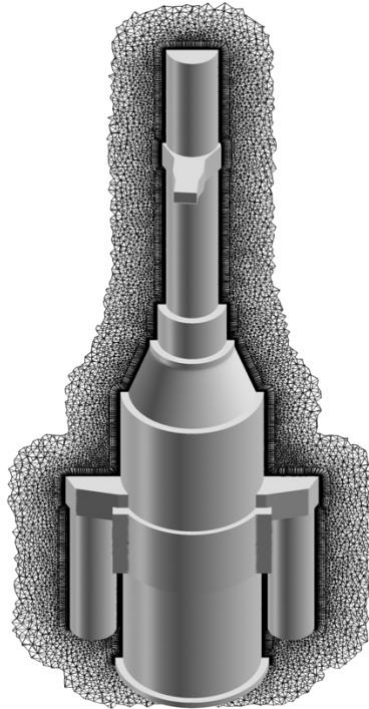
Figure 2.11 Unstructured test stand grid (From Ref. [24]).

From the University of Tennessee, fully turbulent and transition S-76 rotor simulations were performed by Coder [27] to compare two SA-based hybrid RANS/LES turbulence modeling approaches and investigate transition modeling capabilities. The two hybrid approaches used were DDES and Scale-Adaptive Simulation (SAS) [63, 73]. Predictions made using DDES resulted in higher and more accurate figure of merit computations. Predictions with SAS, however, displayed more stable root and tip vortex systems. The root vortex obtained from transition model predictions with DES was cleaner above the blade surface compared to full turbulent predictions, and a figure of merit increase was noticed with the transition simulations. Fully turbulent predictions were also generated by Coder for the PSP rotor [27] which is a rotor of current community interest. The results obtained displayed an increase in instability in the root vortex system as the collective pitch angle was increased. Predictions were not compared to experimental data due to unavailability for the tip Mach number used.

The current work serves as an extension to previous simulations completed by the author [74, 75] utilizing the PSP rotor and ROBIN Mod7 fuselage. Transition simulations conducted at a tip Mach number of 0.65 [74] served as an introduction into transition modeling as experimental data was not available. Transition simulation with the addition of the fuselage [75], however, were compared to available experimental measurements. Both studies assessed hover performance, transition locations, and wake behavior.

2.3 Experimental Overview

As efforts continue to improve turbulence and transition modeling capabilities, experimental data sets are required to determine the accuracy and value that newer models hold. Experimental tests with infrared thermography allow visualization of transition locations as well as hover performance data. Of particular interest, hover experiments utilizing a Mach-scaled rotor [51] were completed in the NASA Langley Research Center Rotor Test Cell (RTC). The experiments were designed to analyze upper and lower blade surface transition locations and hover performance due to boundary layer transition. Figure 2.12 shows the experimental test configuration utilized for the hover tests.
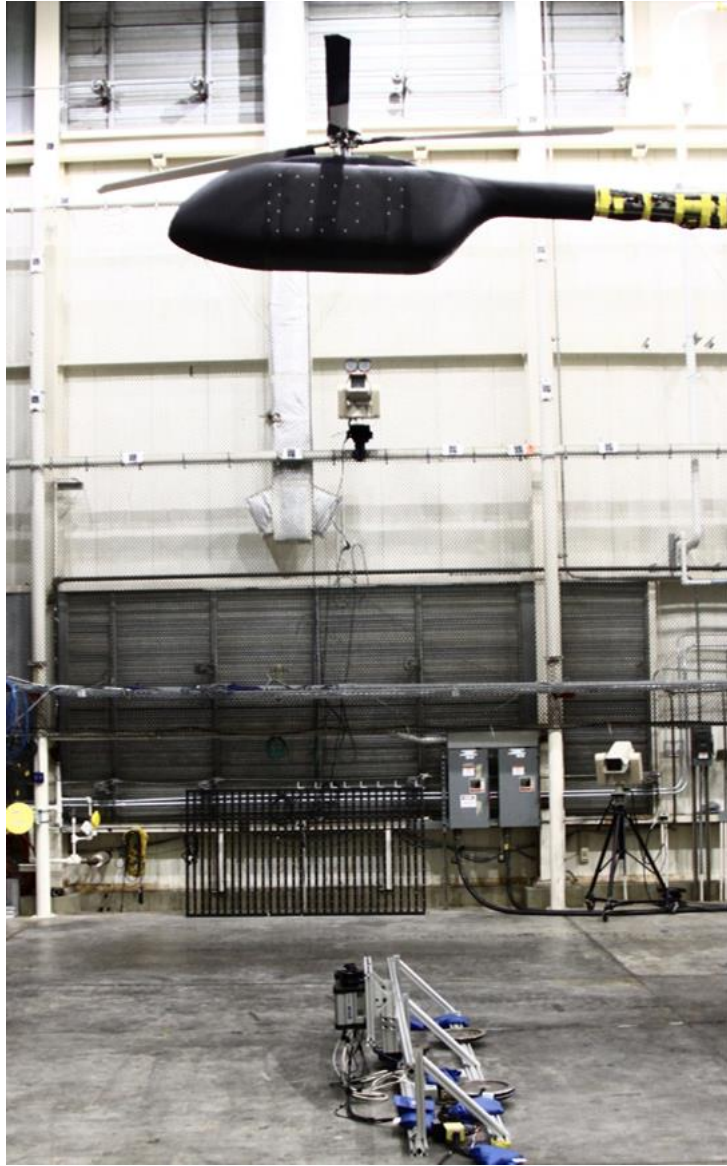
Figure 2.12 Experimental test setup (From Ref. [51]).

The rotor blades utilized for the experiments [51] were specifically selected for PSP validation experiments. Additionally, the hover experiments included ROBIN Mod7 fuselage shell and were completed at a tip Mach number of 0.58. Both forced and natural transition cases were studied. To induce transition, trip dots were used and equally spaced along the upper and lower surfaces. The height of each trip dot was determined based on analysis using BEAR [76] to reduce the drag created by the trip dot itself. Figure 2.13 represents trip dots placed on the lower surface.

Figure 2.13 Trip dot placement along lower blade surface (From Ref. [51]).

Infrared thermography was utilized to visualize the transition locations along the boundary layer. One rotor blade was coated with a specialized paint heater coat which provided the required temperature differential between the surface and the airflow. Transition was visible due to varying surface temperatures between laminar and turbulent boundary layer states [51].

Rotor hover performance was analyzed for both natural and forced transition as shown in Figure 2.14. Forced transition resulted in lower figures of merit for all thrust levels. The results showed how at low thrust, the forced upper surface transition had a greater impact than the forced lower surface transition due to the lower surface being mostly turbulent except near the tip. Perhaps the most significant result of this study was that forcing transition on the upper-surface reduced the figure of merit by 0.02 at high thrusts, even though the blade upper surface is expected to transition upstream of the trip dots. This proved that the effects were due to drag from the trip dots themselves [51].

23
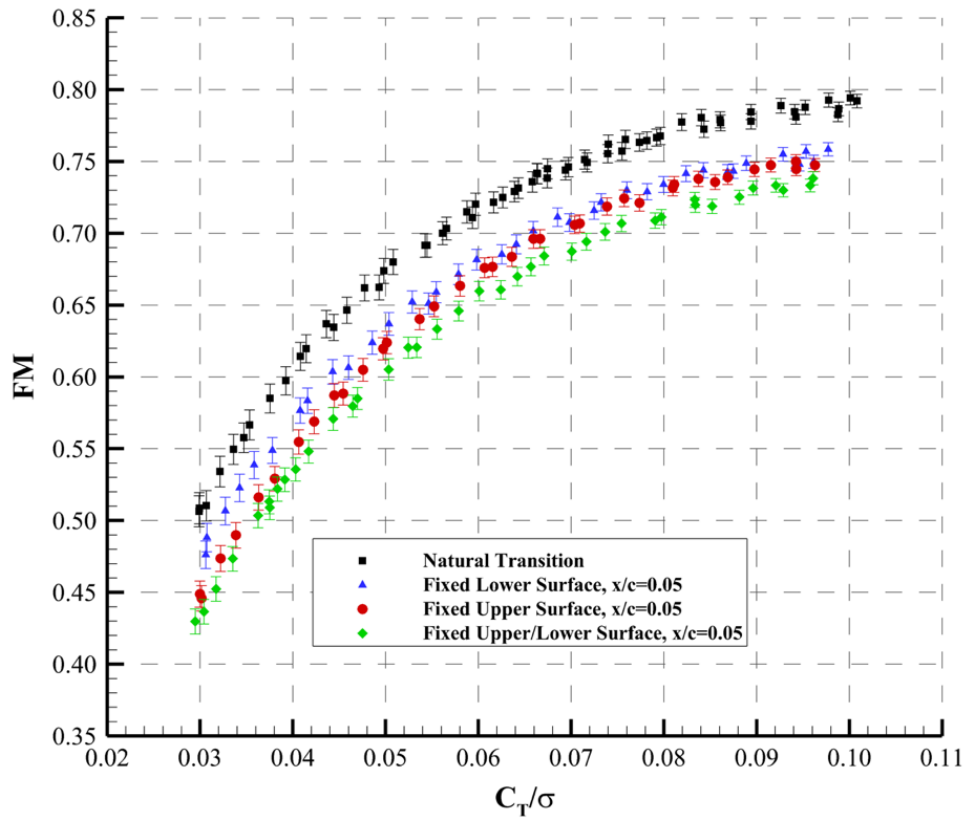
Figure 2.14 PSP hover performance for natural and forced transition (From Ref. [51]).

The completed hover tests [51] were able to provide accurate displays of laminar and turbulent flow on the upper and lower blade surfaces. It was reasoned that the boundary layer can greatly impact hover performance, such as drag due to boundary layer separation. The natural transition case provided quality measurements and transition locations that also aided in determining where to induce transition on forced cases. More studies and tools are still required to completely understand boundary layer effects on transition which will expand CFD modeling capabilities.

CHAPTER 3
COMPUTATIONAL METHODOLOGY

3.1 Governing Equations

The simulations completed in the current study were performed using the OVERFLOW 2.2 [65] compressible flow solver which solves the three-dimensional Navier-Stokes equations in general curvilinear coordinates [77]. The nondimensionalized Navier-Stokes equations are given as

$$\partial_\tau \hat{q} + \partial_\xi \left(\hat{E} - \hat{E}_\nu \right) + \partial_\eta \left(\hat{F} - \hat{F}_\nu \right) + \partial_\zeta \left(\hat{G} - \hat{G}_\nu \right) = 0 \tag{3.1}$$

where the vector composed of conservation variables is defined as

$$\hat{q} = J^{-1} \begin{bmatrix} \rho \\ \rho u \\ \rho v \\ \rho w \\ \rho e_0 \end{bmatrix} \tag{3.2}$$

$$e_0 = C_v T + \frac{1}{2} \left(u^2 + v^2 + w^2 \right) \tag{3.3}$$

in which the Cartesian velocity components are represented by u, v, and w. The total energy is written as e_0, and the density is denoted as ρ. J^{-1} represents the transformation matrix containing the metric terms. The inviscid flux terms are defined as

$$
\hat{E} = J^{-1}
\begin{bmatrix}
\rho U \\
\rho u U + \xi_x p \\
\rho v U + \xi_y p \\
\rho w U + \xi_z p \\
(e + p)\,U - \xi_t p
\end{bmatrix}, \quad
\hat{F} = J^{-1}
\begin{bmatrix}
\rho V \\
\rho u V + \eta_x p \\
\rho v V + \eta_y p \\
\rho w V + \eta_z p \\
(e + p)\,V - \eta_t p
\end{bmatrix}, \quad
\hat{G} = J^{-1}
\begin{bmatrix}
\rho W \\
\rho u W + \zeta_x p \\
\rho v W + \zeta_y p \\
\rho w W + \zeta_z p \\
(e + p)\,W - \zeta_t p
\end{bmatrix}
\tag{3.4}
$$

where p represents the pressure, which is found using the ideal gas law as

$$
p = \rho\,(\gamma - 1)\left[e_0 - \frac{1}{2}\left(u^2 + v^2 + w^2\right)\right]
\tag{3.5}
$$

The contravariant velocity terms, U, V, and W are written as

$$
\begin{aligned}
U &= \xi_t + \xi_x u + \xi_y v + \xi_z w \\
V &= \eta_t + \eta_x u + \eta_y v + \eta_z w \\
W &= \zeta_t + \zeta_x u + \zeta_y v + \zeta_z w
\end{aligned}
\tag{3.6}
$$

which are the finite-differencing equivalent to face-normal velocities. The viscous flux terms utilized in Equation 3.1 are given by

$$
\begin{aligned}
\hat{E}_v &= J^{-1}
\begin{bmatrix}
0 \\
\xi_x \tau_{xx} + \xi_y \tau_{xy} + \xi_z \tau_{xz} \\
\xi_x \tau_{yx} + \xi_y \tau_{yy} + \xi_z \tau_{yz} \\
\xi_x \tau_{zx} + \xi_y \tau_{zy} + \xi_z \tau_{zz} \\
\xi_x \beta_x + \xi_y \beta_y + \xi_z \beta_z
\end{bmatrix} \\[4pt]
\hat{F}_v &= J^{-1}
\begin{bmatrix}
0 \\
\eta_x \tau_{xx} + \eta_y \tau_{xy} + \eta_z \tau_{xz} \\
\eta_x \tau_{yx} + \eta_y \tau_{yy} + \eta_z \tau_{yz} \\
\eta_x \tau_{zx} + \eta_y \tau_{zy} + \eta_z \tau_{zz} \\
\eta_x \beta_x + \eta_y \beta_y + \eta_z \beta_z
\end{bmatrix} \\[4pt]
\hat{G}_v &= J^{-1}
\begin{bmatrix}
0 \\
\zeta_x \tau_{xx} + \zeta_y \tau_{xy} + \zeta_z \tau_{xz} \\
\zeta_x \tau_{yx} + \zeta_y \tau_{yy} + \zeta_z \tau_{yz} \\
\zeta_x \tau_{zx} + \zeta_y \tau_{zy} + \zeta_z \tau_{zz} \\
\zeta_x \beta_x + \zeta_y \beta_y + \zeta_z \beta_z
\end{bmatrix}
\end{aligned}
\tag{3.7}
$$

where the shear stresses and additional terms are defined using

$$
\begin{aligned}
\tau_{xx} &= \lambda \left(u_x + v_y + w_z \right) + 2\mu u_x \\
\tau_{xy} &= \tau_{yx} = \mu \left(u_y + v_x \right) \\
\tau_{xz} &= \tau_{zx} = \mu \left(u_z + w_x \right) \\
\tau_{yy} &= \lambda \left(u_x + v_y + w_z \right) + 2\mu v_y \\
\tau_{yz} &= \tau_{zy} = \mu \left(v_z + w_y \right) \\
\tau_{zz} &= \lambda \left(u_x + v_y + w_z \right) + 2\mu w_z \\
\beta_x &= \gamma \kappa Pr^{-1} \partial_x e_1 + u\tau_{xx} + v\tau_{xy} + w\tau_{xz} \\
\beta_y &= \gamma \kappa Pr^{-1} \partial_y e_1 + u\tau_{yx} + v\tau_{yy} + w\tau_{yz} \\
\beta_z &= \gamma \kappa Pr^{-1} \partial_z e_1 + u\tau_{zx} + v\tau_{zy} + w\tau_{zz} \\
e_1 &= e\rho^{-1} - 0.5 \left(u^2 + v^2 + w^2 \right)
\end{aligned}
\tag{3.8}
$$

The ratio of specific heats and the thermal conductivity coefficient are represented by γ and κ, respectively. Additionally, *Pr* represents the Prandtl number, and μ is the dynamic viscosity. The metric terms acquired to define the generalized form are given as,

$$
\begin{aligned}
\xi_x &= J \left(y_\eta z_\zeta - y_\zeta z_\eta \right) & \eta_x &= J \left(z_\xi y_\zeta - y_\xi z_\zeta \right) \\
\xi_y &= J \left(z_\eta x_\zeta - x_\eta z_\zeta \right) & \eta_y &= J \left(x_\xi z_\zeta - x_\zeta z_\xi \right) \\
\xi_z &= J \left(x_\eta y_\zeta - y_\eta x_\zeta \right) & \eta_z &= J \left(y_\xi x_\zeta - x_\xi y_\zeta \right) \\
\zeta_x &= J \left(y_\xi z_\eta - z_\xi y_\eta \right) & \xi_t &= -x_\tau \xi_x - y_\tau \xi_y - z_\tau \xi_z \\
\zeta_y &= J \left(x_\eta z_\xi - x_\xi z_\eta \right) & \eta_t &= -x_\tau \eta_x - y_\tau \eta_y - z_\tau \eta_z \\
\zeta_z &= J \left(x_\xi y_\eta - y_\xi x_\eta \right) & \zeta_t &= -x_\tau \zeta_x - y_\tau \zeta_y - z_\tau \zeta_z
\end{aligned}
\tag{3.9}
$$

and the transformation matrix is defined as

$$
J^{-1} = x_\xi y_\eta z_\zeta + x_\zeta y_\xi z_\eta + x_\eta y_\zeta z_\xi - x_\xi y_\zeta z_\eta - x_\eta y_\xi z_\zeta - x_\zeta y_\eta z_\xi
\tag{3.10}
$$

3.2 Structured, Overset Grid System

The Mach-scaled PSP blades that are the basis for the current simulations were developed by NASA and the US Army for wind tunnel experiments. The conventional pressure visualization method was to use pressure sensors on the blade surfaces; however, improvements were made by applying pressure sensitive paint to the blades. The blades utilized for the hover experiments were acquired from previous hover tests, and the

measurements were performed in NASA Langley's RTC by Overmeyer and Martin [51]. The blade planform was designed utilizing government RC-series airfoils as pictured in Figure 3.1 [52], and pertinent blade properties are listed in Table 3.1 [52].

In addition to the PSP rotor blades, the ROBIN Mod7 fuselage shell was utilized for the current study. The wind-tunnel model was developed as a simple transport helicopter design and was also utilized for hover tests completed by Overmeyer and Martin [51]. For the current simulations and the hover experiments, the rotor shaft position was set at -3.5° nose down. Figure 3.2 represents the fuselage shell's dimensions.
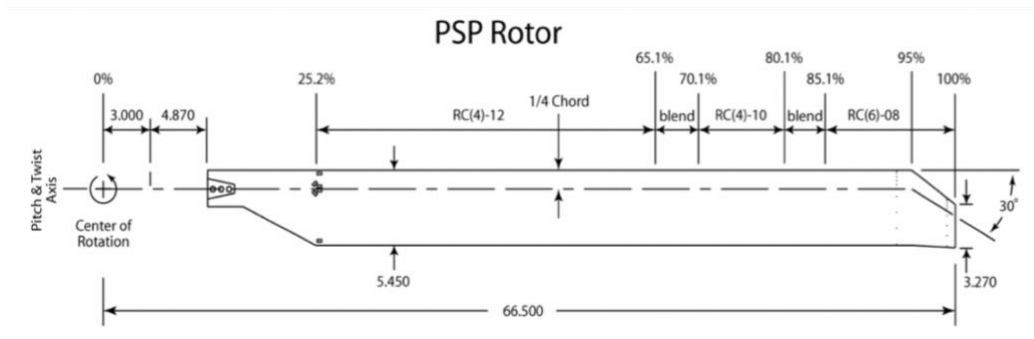
Figure 3.1 PSP blade planform definition (From Ref. [52]).

Table 3.1 PSP Rotor Properties (From Ref. [52]).

Number of Blades, N_b	4
Radius, R	66.50"
Chord, c	5.45"
Solidity, σ	0.1033
Twist	-14°
Tip taper	0.60
Tip sweep	30° ($c/4$)
Airfoils	RC(4)-10
	RC(4)-12
	RC(6)-8

29
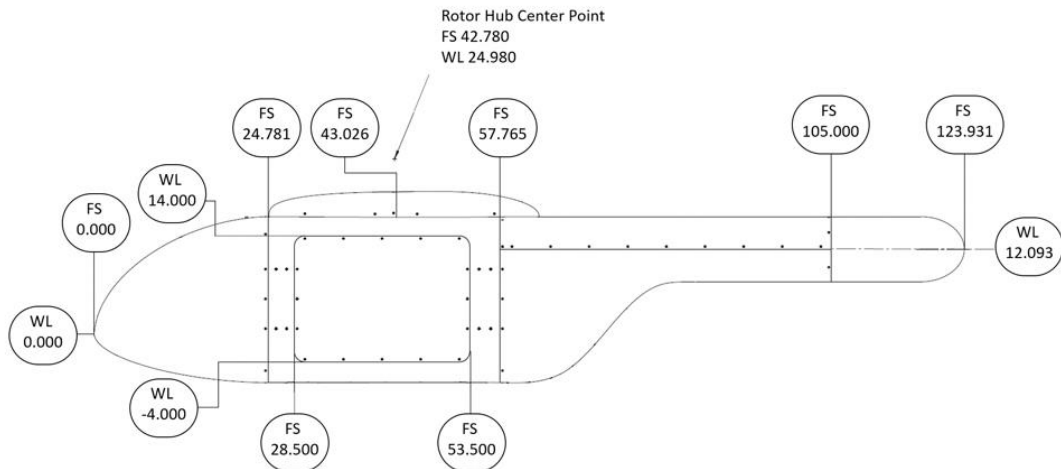
Figure 3.2 ROBIN Mod7 fuselage basic dimensions (From Ref. [51]).

3.2.1 Near-Body Grid Generation

Simulations were completed utilizing structured, overset grids for both the PSP rotor and the ROBIN fuselage. Surface grids for the rotor were provided by the AIAA Applied Aerodynamics Technical Committee's Rotorcraft Simulations and Performance Predictions discussion group. The provided grids represented a single blade with three overset grids: the main blade section, a hub cap, and a tip cap. These individual grids were duplicated to generate the other blades.

The fuselage surface meshes were generated in Pointwise [78] based on an IGES file provided by Overmeyer and Martin. This grid system was generated to feature three meshes for the main body, three meshes around the hub, and a collar grid connecting the two. For both the hub and fuselage body, a grid was created at the fore and aft locations to avoid any singularities. The collar grid was used to ensure overset connectivity between the hub and fuselage body. The collar was constructed with SURGRD, a program provided within Chimera Grid Tools [61].

HYPGEN, another program available within Chimera Grid Tools [61], was used to generate the volume grids for both the rotor blades and fuselage. The tip Mach number selected was 0.58 to match the experimental conditions which corresponded to a Reynolds number per inch of 3.84×10^5. The initial wall spacing for both grids was determined based

30

on a y+ value of 0.67 taken at the blade tip and was approximately 3.45 x 10^{-5} inches. To maintain a reasonable stretching ratio, 65 surface-normal points were utilized for the two grid systems. The blade grids were extruded 6 inches from the surface as shown in Figure 3.3, and the fuselage grid was extruded 9 inches from the surface as displayed in Figure 3.4. The blades were generated with roughly 11 million points per blade totaling approximately 44 million points for the PSP grid, and the fuselage grid system was created using about 10 million grid points.
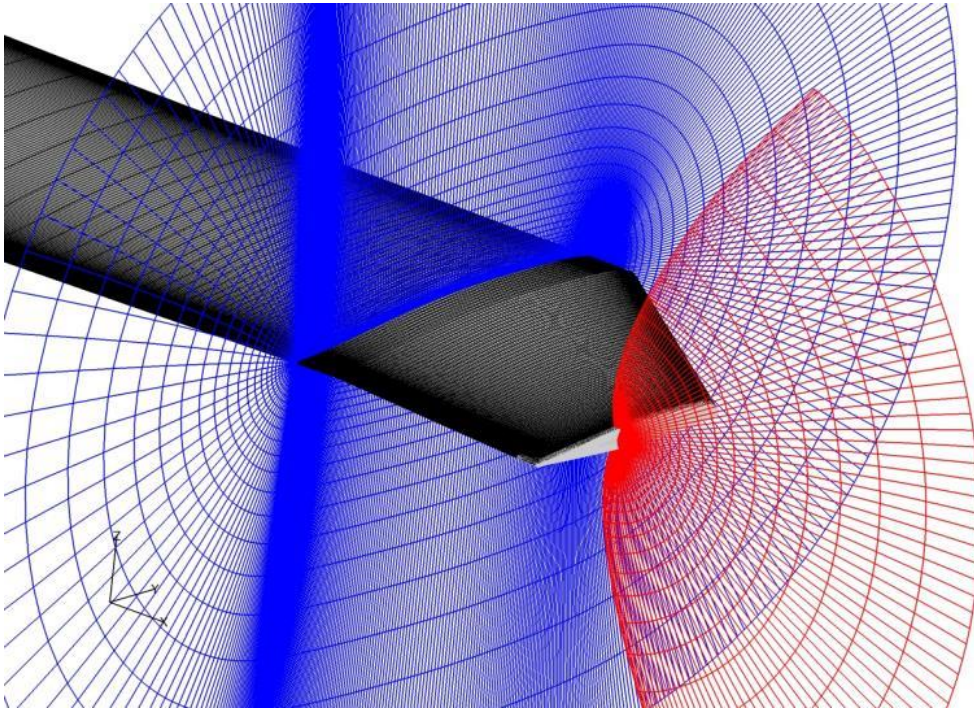
Figure 3.3 PSP rotor grid system.
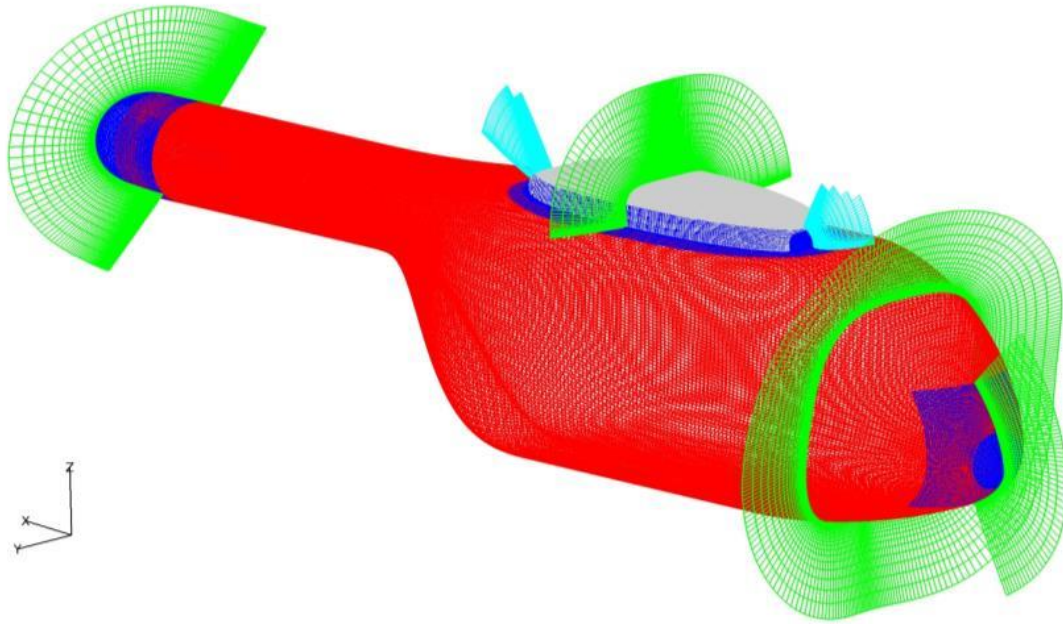
Figure 3.4 ROBIN fuselage overset grid system.

3.2.2 Off-Body Grid Generation

A nested Cartesian background mesh was selected as the off-body grid method for both simulations with and without the fuselage to capture significant flow features. Both meshes were created automatically through inputs in OVERFLOW as seen in Figure 3.5. For the isolated rotor, the off-body mesh was developed using near-field brick dimensions of 150″x150″x60″, and the rotor-fuselage grid dimensions were slightly altered to adjust for the extended tail region. The rotor-fuselage brick dimensions were 165″x150″x60″. The near-field brick spacing was selected to be 0.5″, which is approximately 9.2% of the chord length, and the grids coarsen as they extend to far-field boundaries. The PSP off-body grid system was generated using roughly 15.3 million points, and the rotor-fuselage off-body grid was constructed with approximately 16.5 million points.
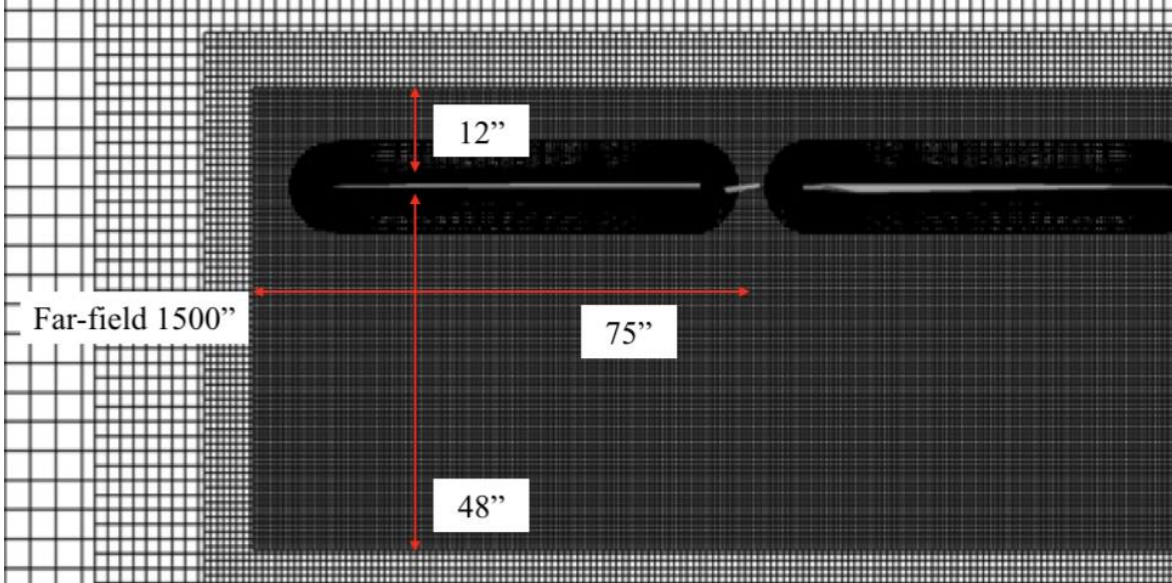
(a)
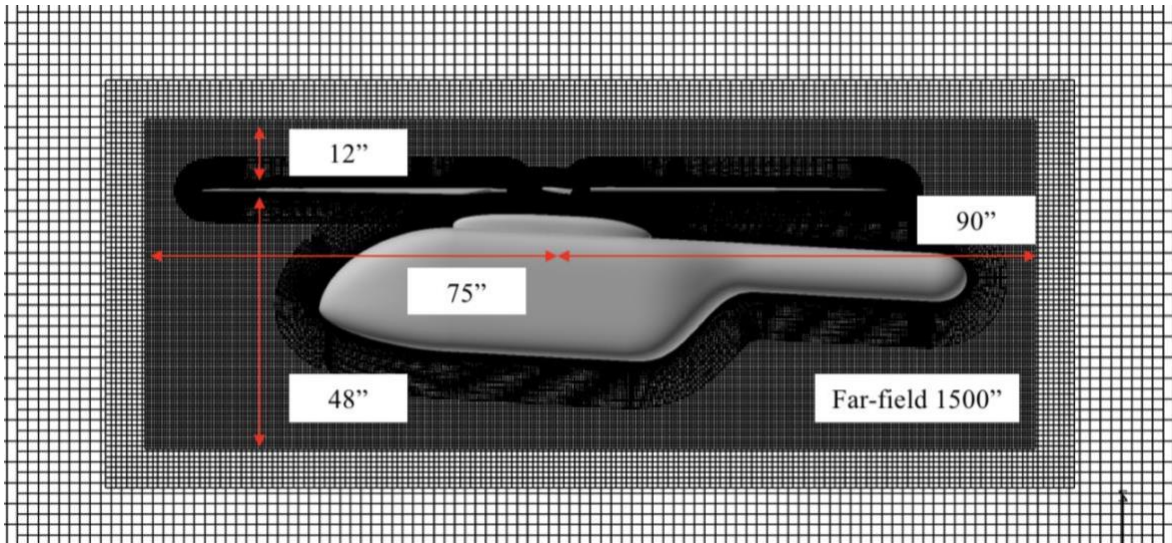
(b)

Figure 3.5 Isolated rotor and rotor-fuselage off-body grid systems.

3.3 NASA OVERFLOW Code

Transition simulations utilizing the grids described above were completed with the OVERFLOW 2.2 compressible flow solver [65]. The solver is a structured, overset RANS code developed and maintain by NASA. The code is capable of simulating multiple moving bodies and time-accurate simulations. Additionally, the solver offers various implicit schemes, multiple high-order flux discretization methods, and several turbulence and transition models. For the current studies, the Roe flux-difference splitting algorithm (IRHS=4) [79] along with a 5th-order-acccurate Weighted Essentially Non-Oscillatory (WENO) [80] reconstruction was used. To ensure efficient inversion and stable simulations, the Diagonalized Diagonal Dominant Alternating Direction Implicit (D3ADI) scheme [81] was applied.

3.3.1 Roe Flux-Difference Splitting Scheme

The Roe flux-difference splitting scheme [79] was used for the simulations in this thesis in order to calculate the fluxes between nodes and appropriately penalize discontinuous jumps. The total flux difference is written as

$$\frac{dF}{d\xi} = F_{i+\frac{1}{2}} - F_{i-\frac{1}{2}} \tag{3.11}$$

and the left and right flux waves are approximated using

$$F_{i+\frac{1}{2}} = \frac{1}{2}\left(F_R + F_L\right) - \frac{1}{2}\left|\hat{A}\right|\left(q_R - q_L\right) \tag{3.12}$$

The difference for each side is reduced into summations given as

$$\left|\hat{A}\right| = \hat{T}\left|\hat{\lambda}\right|\hat{T}^{-1} \tag{3.13}$$

34

The hat characters indicate that the terms are constructed using the so-called Roe-averaged values of the left and right states. This averaging allows exact capturing of shockwaves and the Rankine-Hugoniot relations.

3.3.2 Weighted Essentially Non-Oscillatory (WENO) Spatial Discretization

The 5th-order WENO reconstruction applied for this study is achieved using three 2rd-order estimations as pictured in Figure 3.6 [80], and this interpolation scheme allows high order spatial discretization and relieves extensive oscillatory behavior. The methodology used follows the work of Henrick et al. [82] and Merriman [83] in which the left and right variables are defined as

$$\hat{q}^L_{i+\frac{1}{2}} = w^L_0 \hat{q}^{L0}_{i+\frac{1}{2}} + w^L_1 \hat{q}^{L1}_{i+\frac{1}{2}} + w^L_2 \hat{q}^{L2}_{i+\frac{1}{2}} \qquad (3.14)$$

and

$$\hat{q}^R_{i+\frac{1}{2}} = w^R_0 \hat{q}^{R0}_{i+\frac{1}{2}} + w^R_1 \hat{q}^{R1}_{i+\frac{1}{2}} + w^R_2 \hat{q}^{R2}_{i+\frac{1}{2}} \qquad (3.15)$$

The 2rd-order approximations for the left and right variables are created from the individual nodes and written as

$$\begin{aligned}
\hat{q}^{L0}_{i+\frac{1}{2}} &= \tfrac{1}{3}q_{i-2} - \tfrac{7}{6}q_{i-1} + \tfrac{11}{6}q_i \\
\hat{q}^{L1}_{i+\frac{1}{2}} &= -\tfrac{1}{6}q_{i-1} + \tfrac{5}{6}q_i + \tfrac{1}{3}q_{i+1} \\
\hat{q}^{L2}_{i+\frac{1}{2}} &= \tfrac{1}{3}q_i + \tfrac{5}{6}q_{i+1} - \tfrac{1}{6}q_{i+2}
\end{aligned} \qquad (3.16)$$

and

$$\hat{q}_{i+\frac{1}{2}}^{R0} = \tfrac{1}{3}q_{i+3} - \tfrac{7}{6}q_{i+2} + \tfrac{11}{6}q_{i+1}$$
$$\hat{q}_{i+\frac{1}{2}}^{R1} = -\tfrac{1}{6}q_{i+2} + \tfrac{5}{6}q_{i+1} + \tfrac{1}{3}q_i \qquad (3.17)$$
$$\hat{q}_{i+\frac{1}{2}}^{R2} = \tfrac{1}{3}q_{i+1} + \tfrac{5}{6}q_i - \tfrac{1}{6}q_{i-1}$$
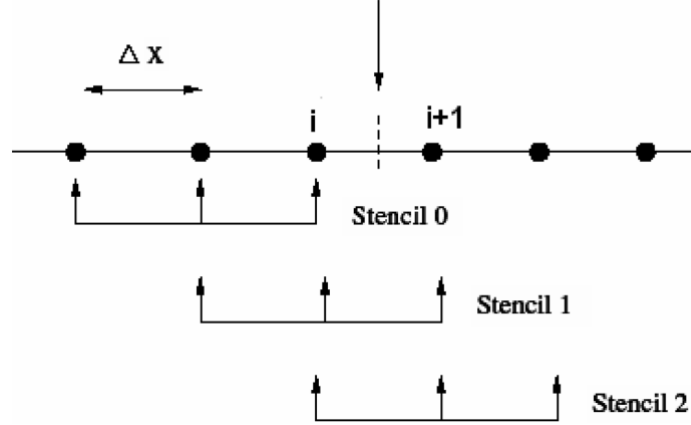
Figure 3.6 5th-order WENO reconstruction stencil (From Ref. [80]).

To reduce numerical dissipation and achieve a true 5th-order spatial discretization, it is desired for adjusted weight values (w) to achieve optimal weights values (γ_k). The specific optimal weights are $\gamma_0 = 0.1$, $\gamma_1 = 0.6$, and $\gamma_2 = 0.3$, and the adjusted weights are given as

$$\tilde{w}_k = \frac{\gamma_k}{(\varepsilon + \beta_k)^2} \qquad (3.18)$$

To track and account for stencils that cause the adjusted weights to deviate from ideal values, smoothness gauges (β_k) are utilized for the left and right variables and are defined as

$$\beta_0^L = \tfrac{13}{12}\left(q_{i-2} - 2q_{i-1} + q_i\right)^2 + \tfrac{1}{4}\left(q_{i-2} - 4q_{i-1} + 3q_i\right)^2$$
$$\beta_1^L = \tfrac{13}{12}\left(q_{i-1} - 2q_i + q_{i+1}\right)^2 + \tfrac{1}{4}\left(q_{i-1} - q_{i+1}\right)^2 \qquad (3.19)$$
$$\beta_2^L = \tfrac{13}{12}\left(q_i - 2q_{i+1} + q_{i+2}\right)^2 + \tfrac{1}{4}\left(3q_i - 4q_{i+1} + q_{i+2}\right)^2$$

and

$$\begin{aligned}
\beta_0^R &= \tfrac{13}{12}\left(q_{i+3} - 2q_{i+2} + q_{i+1}\right)^2 + \tfrac{1}{4}\left(q_{i+3} - 4q_{i+2} + 3q_{i+1}\right)^2 \\
\beta_1^R &= \tfrac{13}{12}\left(q_{i+2} - 2q_{i+1} + q_i\right)^2 + \tfrac{1}{4}\left(q_{i+2} - q_i\right)^2 \\
\beta_2^R &= \tfrac{13}{12}\left(q_{i+1} - 2q_i + q_{i-1}\right)^2 + \tfrac{1}{4}\left(3q_{i+1} - 4q_i + q_i\right)^2
\end{aligned} \tag{3.20}$$

3.3.3 Diagonalized Diagonal Dominant Alternating Direction Implicit (D3ADI) Scheme

The D3ADI scheme [81] was employed for the current work which extends on the DDADI scheme of Bardina and Lombard [84]. The scheme utilizes the diagonalization technique of Pulliam and Chaussee [85] for the inviscid flux terms but also entails estimating values to achieve scalar diagonals which increases possible estimation errors compared to base schemes. The estimation error is revised with the addition of Hunag sub-iterations allowing efficient computation power and stability while maintaining acceptable time requirements.

3.3.4 Spalart-Allmaras Turbulence Model

The turbulence model selected for the current simulations was the one equation Spalart-Allmaras (SA) eddy viscosity model [32], more specifically, the SA-neg variant [86] with the application of the Spalart-Shur rotation/curvature correction [64]. The model is based on the Boussinesq eddy-viscosity hypothesis where the Reynolds stresses are given as

$$-\overline{u_i u_j} = 2\mu_t\left(S_{ij} - \frac{1}{3}\frac{\partial u_k}{\partial x_k}\delta_{ij}\right) - \frac{2}{3}\rho k \delta_{ij} \tag{3.21}$$

in which the second term on the right-hand side containing the turbulent kinetic energy (k) is neglected in OVERFLOW for one-equation turbulence models. The strain-rate tensor (S_{ij}) is defined based on the mean velocity (U) and written as

$$S_{ij} \equiv \frac{1}{2}\left(\frac{\partial U_i}{\partial x_j} + \frac{\partial U_j}{\partial x_i}\right) \tag{3.22}$$

The eddy viscosity, ν_t, is broken down as a function of the molecular viscosity (ν) and the variable of interest ($\tilde{\nu}$) and is given as

$$\nu_t = \tilde{\nu} f_{\nu 1}, \quad f_{\nu 1} = \frac{\chi^3}{\chi^3 + c_{\nu 1}^3}, \quad \chi = \frac{\tilde{\nu}}{\nu} \tag{3.23}$$

The turbulence working variable ($\tilde{\nu}$) is found through solution of a transport equation,

$$\frac{D\tilde{\nu}}{Dt} = c_{b1}\tilde{S}\left(1 - f_{t2}\right)\tilde{\nu} - \left(c_{w1}f_w - \frac{c_{b1}}{\kappa^2}f_{t2}\right)\left(\frac{\tilde{\nu}}{d}\right)^2 + \frac{1}{\sigma}\left\{\frac{\partial}{\partial x_j}\left[(\nu + \tilde{\nu})\frac{\partial \tilde{\nu}}{\partial x_j}\right] + c_{b2}\frac{\partial \tilde{\nu}}{\partial x_j}\frac{\partial \tilde{\nu}}{\partial x_j}\right\} \tag{3.24}$$

in which

$$\tilde{S} \equiv S + \frac{\tilde{\nu}}{\kappa^2 d^2}f_{\nu 2}, \quad f_{\nu 2} = 1 - \frac{\chi}{1 + \chi f_{\nu 1}} \tag{3.25}$$

where d represents the space to the closest surface. The f_{t2} function is used to facilitate transition modeling which will be discussed in the next section. The f_w function is defined as

$$f_w = g\left[\frac{1 + c_{w3}^6}{g^6 + c_{w3}^6}\right]^{\frac{1}{6}}, \quad g = r + c_{w2}\left(r^6 - r\right), \quad r \equiv \frac{\tilde{\nu}}{\tilde{S}\kappa^2 d^2} \tag{3.26}$$

The constants from the transport equation are $c_{b1} = 0.1355$, $c_{b2} = 0.622$, $\sigma = 2/3$, $\kappa = 0.41$, $c_{\nu 1} = 7.1$, $c_{w2} = 0.3$, $c_{w3} = 2$, and

$$c_{w1} = \frac{c_{b1}}{\kappa^2} + \frac{1 + c_{b2}}{\sigma} \tag{3.27}$$

A hybrid RANS/LES capability is introduced through the addition of Delayed, Detached Eddy Simulation (DDES) [63]. This influences RANS behavior for attached boundary layers by modifying the length scale and converts to LES behavior for separated shear regions and wake structures. To apply this methodology, the length scale is modified in the transport equation as

$$d \to \tilde{d} - f_d \max\left(0, d - C_{DES}\Delta\right) \tag{3.28}$$

where the calibration coefficient (C_{DES}) is set to 0.65.

3.3.5 Amplification Factor Transport Transition Model (AFT2017b)

The effects of laminar-turbulent transition are captured using the AFT2017b transition model of Coder [27] and Coder and Maughmer [28]. The transition model is coupled to the SA eddy viscosity model and requires the solution of two additional transport equations. The first is the amplification factor, given as

$$\frac{\partial\left(\rho\tilde{n}\right)}{\partial t} + \frac{\partial\left(\rho u_j\tilde{n}\right)}{\partial x_j} = \rho\Omega F_{crit}F_{growth}\frac{d\tilde{n}}{dRe_\theta} + \frac{\partial}{\partial x_j}\left[\left(\mu + \sigma_n\mu_t\right)\frac{\partial\tilde{n}}{\partial x_j}\right] \tag{3.29}$$

and the second is the modified intermittency, written as

$$\frac{\partial\left(\rho\tilde{\gamma}\right)}{\partial t} + \frac{\partial\left(\rho u_j\tilde{\gamma}\right)}{\partial x_j} = c_1\rho S F_{onset}\left[1 - exp\left(\tilde{\gamma}\right)\right] - c_2\rho\Omega F_{turb}\left[c_3 exp\left(\tilde{\gamma}\right) - 1\right] + $$
$$\frac{\partial}{\partial x_j}\left[\left(\mu + \frac{\mu_t}{\sigma_\gamma}\right)\frac{\partial\tilde{\gamma}}{\partial x_j}\right] \tag{3.30}$$

in which μ represents the molecular viscosity, and Ω represents the vorticity magnitude. Also, the diffusion coefficient (σ_n) is set to 1.0. The amplification factor transport equation is used to define boundary-layer behavior as instabilities expand in this region due to transition forced by separation. To account for the development of the envelope amplification factor, an integral shape factor describing the boundary-layer is estimated as

$$H_{12} = 0.376960 + \sqrt{\frac{H_L + 2.453432}{0.653181}} \tag{3.31}$$

which is based on the local shape factor given as

$$H_L = \frac{d^2}{\mu} \left[\nabla \left(\rho \vec{u} \cdot \nabla d \right) \cdot \nabla d \right] \tag{3.32}$$

The effect of critical Reynolds number is introduced using the F_{crit} function,

$$F_{crit} = \begin{cases} 0, Re_V < Re_{V,0} \\ 1, Re_V \geq Re_{V,0} \end{cases} \tag{3.33}$$

$$Re_V = \frac{\rho S d^2}{\mu + \mu_t} \tag{3.34}$$

$$\frac{Re_{V,0}}{Re_{\theta,0}} = 0.246175 H_{12}^2 - 0.141831 H_{12} + 0.008886 \tag{3.35}$$

$$\log_{10} \left(Re_{\theta,0} \right) = 0.7 \tanh \left(\frac{14}{H_{12} - 1} - 9.24 \right) + \frac{2.492}{\left(H_{12} - 1 \right)^{0.43}} + 0.62 \tag{3.36}$$

The effects of the growth of the boundary-layer itself is modeled using the F_{growth} function.

$$F_{growth} = \frac{H_{12}}{0.5482 H_{12} - 0.5185} \left[1 + m \left(H_{12} \right) \right] \frac{l \left(H_{12} \right)}{2} \tag{3.37}$$

where

$$l \left(H_{12} \right) = \frac{6.54 H_{12} - 14.07}{H_{12}^2} \tag{3.38}$$

$$m(H_{12}) = \left(0.058 \frac{(H_{12} - 4)^2}{H_{12} - 1} - 0.068 \right) \frac{1}{l(H_{12})} \qquad (3.39)$$

and

$$\frac{d\tilde{n}}{dRe_\theta} = 0.028(H_{12} - 1) - 0.0345 exp\left[-\left(\frac{3.87}{H_{12} - 1} - 2.52 \right)^2 \right] \qquad (3.40)$$

which come from Drela and Giles [87]. The modified intermittency from the transport equation represents the natural logarithm of the intermittency which is based on the work of Menter's one-equation transition model [29]. The functions defining the transport equation are given as

$$F_{onset,1} = \min\left(\frac{\tilde{n}}{N_{crit}}, 2 \right) \qquad (3.41)$$

$$F_{onset,2} = \max\left[1 - \left(\frac{\mu_t}{3.5\mu} \right)^3, 0 \right] \qquad (3.42)$$

$$F_{onset} = \max\left[F_{onset,1} - F_{onset,2}, 0 \right] \qquad (3.43)$$

$$F_{turb} = exp\left[-\left(\frac{\mu_t}{2\mu} \right)^4 \right] \qquad (3.44)$$

The critical amplification factor (N_{crit}) represents the maximum allowable amplification before transition and is determined using a modified form of Mack's relation [88]

$$N_{crit} = -8.43 - 2.4ln\left(\frac{\tau}{100} \right) \qquad (3.45)$$

where a restriction is placed on turbulence concentration by using τ which is a function of free-stream turbulence (τ_∞) and is given as

$$\tau = 2.5 tanh \left(\frac{Tu_\infty\,(\%)}{2.5} \right) \qquad (3.46)$$

This modification form was originally suggested by Drela [89]. The provided calibration constants for the modified intermittency transport equation are $c_1 = 100$, $c_2 = 0.06$, $c_3 = 50$, and $\sigma_\gamma = 1.0$.

In order to incorporate the transition model into the turbulence model (SA-neg-RC-AFT2017b), the f_{t2} function (Equation 3.24) is redefined from its original form as

$$f_{t2} = c_{t3} \left[1 - exp\left(\tilde{\gamma}\right) \right] \qquad (3.47)$$

DDES [63] was applied to the simulations (SA-neg-RC-AFT2017b-DDES) by modifying the length scale once again to introduce a hybrid RANS/LES. However, directly utilizing the DDES methodology causes issues with RANS behavior in attached boundary layers and LES behavior for separated flows. To account for this problem, the traditional length scale is altered using a solution-based sensor, f_d, and is defined as

$$\tilde{d} \equiv d - \gamma f_d \max\left(0, d - C_{DES}\Delta\right) \qquad (3.48)$$

where the intermittency (γ) represents the exponential of the modified intermittency from the transport equation.

CHAPTER 4
RESULTS AND DISCUSSION

Results for both the isolated PSP rotor and the PSP rotor with the ROBIN fuselage were obtained with the OVERFLOW 2.2 compressible flow solver as discussed earlier, and the data was analyzed at varying collective pitch angles for both configurations. Turbulence and transition were modeled using SA-neg-RC-AFT2017b-DDES. This chapter will discuss the quantitative and qualitative results acquired in terms of transition locations, rotor performance, and transition modeling capabilities. Additionally, fuselage effects seen in transition predictions will be assessed, and the results will be compared to experimental data for validation. For consistency, a total of 15 revolutions were completed for all simulations.

4.1 Numerical Simulation Strategy

Hover simulations for both the isolated PSP rotor and the PSP rotor with the ROBIN fuselage were completed at collective pitch angles of 4°, 8°, and 10°. Simulations with and without the fuselage at a 4° collective pitch angle were initialized utilizing a global time step corresponding to 1° of rotation, and this condition was applied until 10 revolutions were completed. This allowed the initial transients to advect away. The time step was then modified to represent a 0.25° of rotation for an additional 5 revolutions to further improve the solution quality and effectively capture transition effects. Hover cases with and without the fuselage at collective pitch angles of 8° and 10° were simulated using a time step representing a 0.25° of rotation from startup to maintain numerical stability. Fifteen total revolutions were also completed for these hover simulations to allow thrust and torque convergence. Additionally, to ensure efficient convergence and reduce linearization error, 20 sub-iterations were used for all simulations.

4.2 Isolated Rotor

To analyze performance for the isolated rotor computations, thrust and torque predictions were examined. Table 4.1 displays the thrust and torque average values and standard deviations acquired for the isolated rotor at varying collective pitch angles for the final revolution. Figure of merit was determined using

$$FOM = \sqrt{C_T} \left(\frac{C_T}{C_Q} \right) \qquad (4.1)$$

as a function of rotor thrust (C_T) and torque (C_Q) coefficients. Figure of merit was shown to grow as thrust increased with greater collective pitch. Measured values were compared against predicted figure of merit for collective pitch angles of 8° and 10°. Approximately a 1.15% difference was calculated between the predicted and measured figure of merit for a collective pitch angle of 8°, and roughly a 3.39% error was computed for a collective pitch angle of 10°. Possible reasons for the significant underprediction in figure of merit for the 10° collective pitch case are both uncertainties in measured data due to facility effects and modeling errors in the simulation. It was also noted that measurements were made with the fuselage configuration which, as will be shown, accounts for higher thrust values.

Figures 4.1-3 display the thrust and torque unsteady behaviors against time step for the isolated rotor configuration at varying collective pitch angles. The data displayed represented the final two revolutions, and all cases exhibited fair convergence. Thrust and torque convergence for the 4° collective pitch case using the flow initialization at a 1° of rotation per time step strategy converged as well as the other cases. The 8° thrust and torque history seems to show a slight spike in the data, but this feature is only due to the larger scale compared to the 4° and 10° convergence plots.

Table 4.1 Average Values of PSP Rotor Hover Predictions.

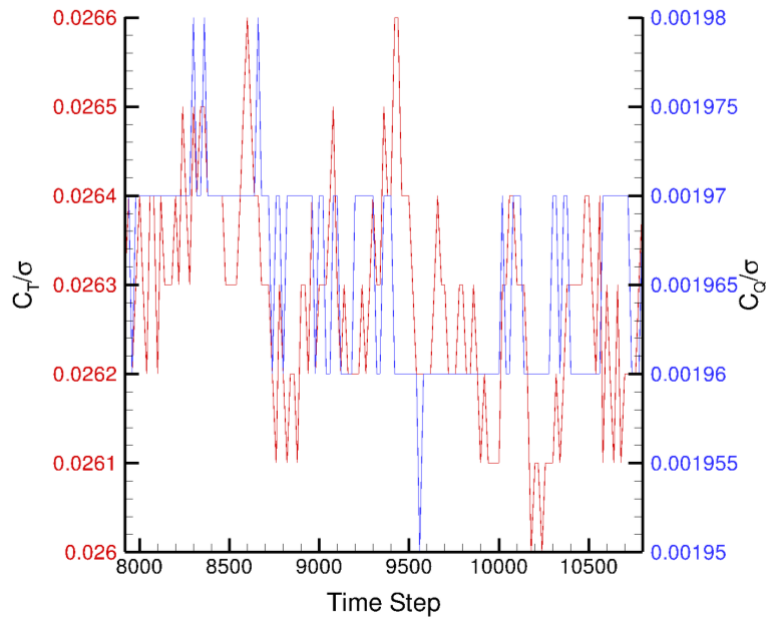| Collective, θ	C_T/σ	C_Q/σ	FM
4°	0.0262 ∓ 0.000118	0.00196 ∓ 0.00000456	0.492 ∓ 0.00319
8°	0.0611 ∓ 0.000262	0.00480 ∓ 0.0000113	0.714 ∓ 0.00385
10°	0.0821 ∓ 0.000144	0.00717 ∓ 0.00000977	0.745 ∓ 0.00161

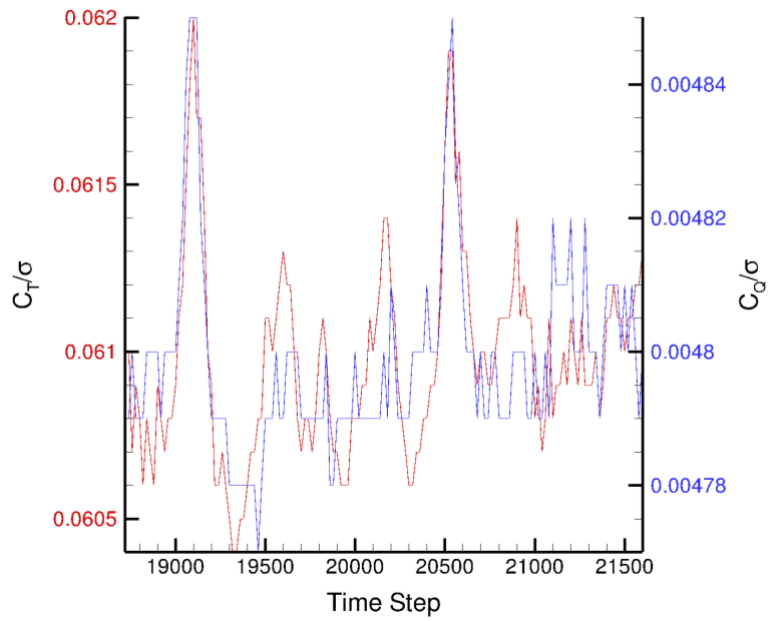Figure 4.1 Thrust and torque convergence history for a 4° collective pitch.

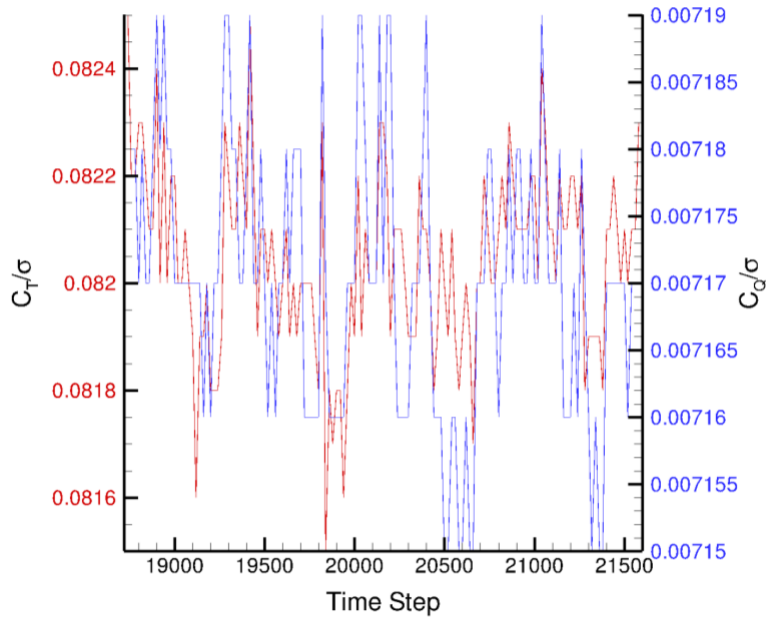Figure 4.2 Thrust and torque convergence history for an 8° collective pitch.

Figure 4.3 Thrust and torque convergence history for a 10° collective pitch.

46

The predicted transition locations were evaluated by comparing the blade surface vorticity magnitude shown in Figures 4.4-6. Transition lines for the 8° collective pitch case based on the average thrust obtained matched measured transition lines fairly well on the upper surface, however, the predicted transition line experienced a greater delayed transition patch closer to the blade tip than the measured results. This trend was also noticed in previous simulations by Jain [46] as shown in Figure 4.7. The two measured transition patches on the lower surface were also not as prominent on the predicted transition locations. Blade surface transition locations at a 10° collective pitch followed measured locations except for a few small trips on the lower surface. Similar differences on the lower surface were also noticed in Jain's predictions. Transition locations were also clearly shown using Spalart's Turbulence Index [32] as seen in Figures 4.8-10. Transition disturbances were noticed near the blade tip possibly due to unsteady tip vortex generation. The measured transition locations for thrust values corresponding to 8° and 10° collective pitches are shown in Figures 4.11 and 4.12 [51].
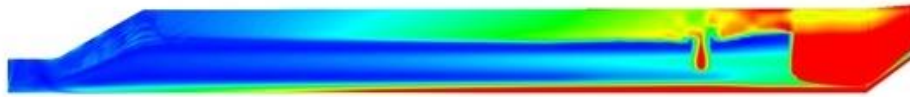
(a)
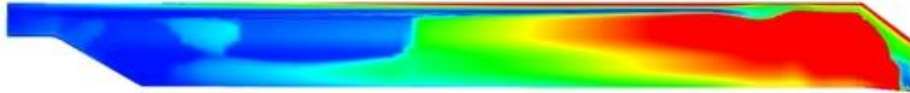
(b)

Figure 4.4 Blade surface vorticity magnitude contours at a 4° collective pitch for the (a) upper surface and the (b) lower surface.

(a)

(b)

Figure 4.5 Blade surface vorticity magnitude contours at an 8° collective pitch for the (a) upper surface and the (b) lower surface.
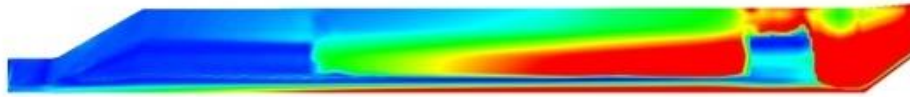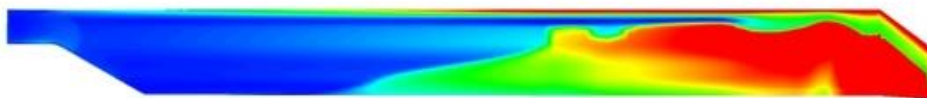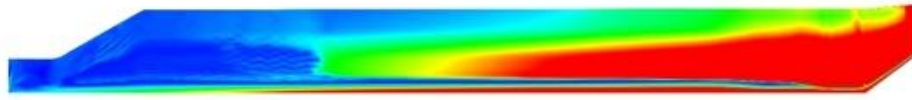
(a)
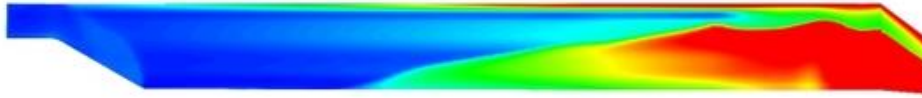
(b)

Figure 4.6 Blade surface vorticity magnitude contours at a 10° collective pitch for the (a) upper surface and the (b) lower surface.
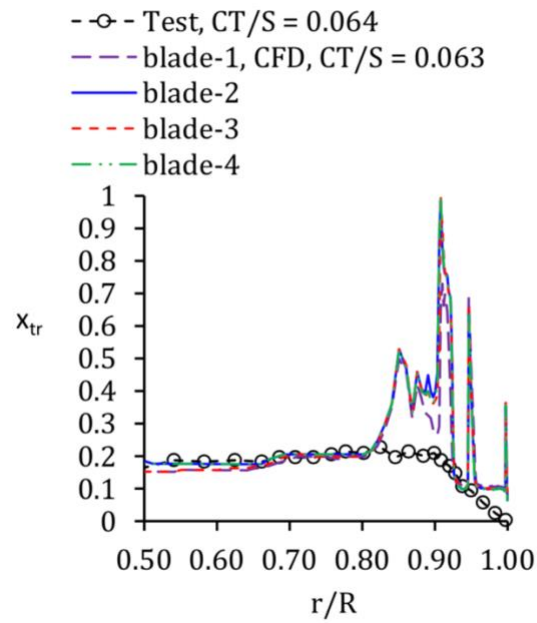
Figure 4.7 Upper surface transition locations for an 8° collective pitch (From Ref. [46]).

(a)

(b)

Figure 4.8 Spalart's Turbulence Index at a 4° collective pitch for the (a) upper surface and the (b) lower surface.

(a)

(b)

Figure 4.9 Spalart's Turbulence Index at an 8° collective pitch for the (a) upper surface and the (b) lower surface.

(a)

(b)

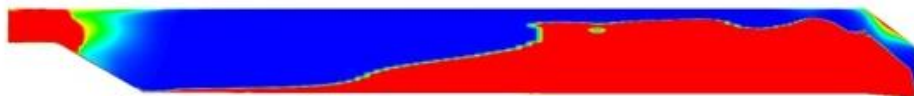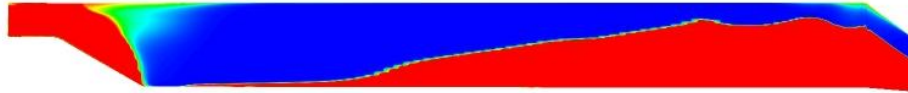Figure 4.10 Spalart's Turbulence Index at a 10° collective pitch for the (a) upper surface and the (b) lower surface.
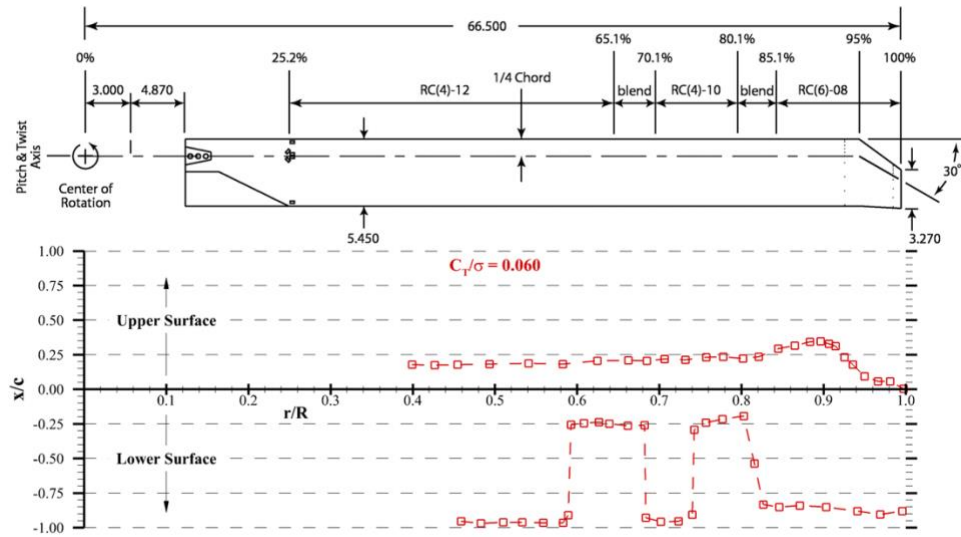

Figure 4.11 Upper and lower surface transition locations for a thrust value corresponding to an 8° collective pitch (From Ref. [51]).
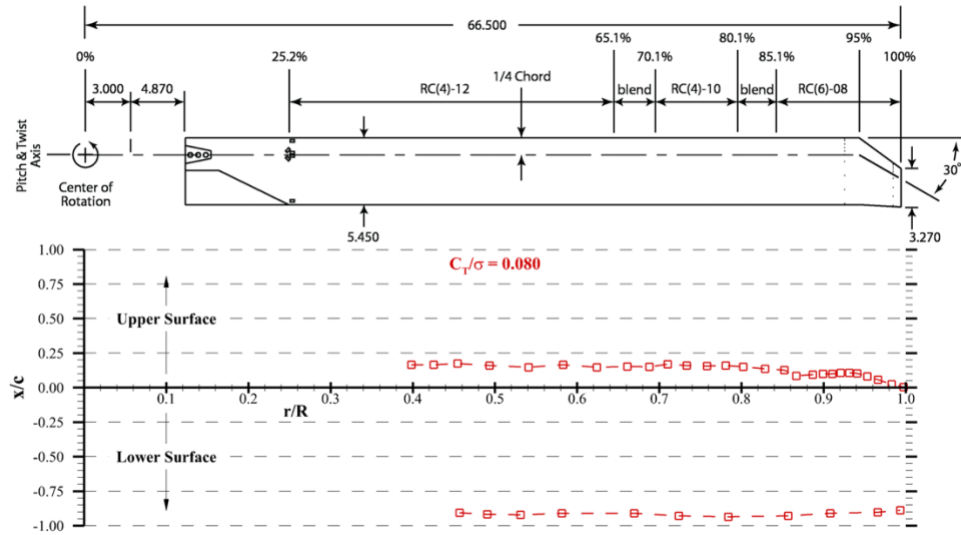
Figure 4.12 Upper and lower surface transition locations for a thrust value corresponding to a 10° collective pitch (From Ref. [51]).

Wake structures for the varying collective pitch angles were examined by creating vorticity magnitude contours on a constant-y center plane as shown in Figures 4.13-15. Vortex wake helps to describe the flow behavior that affects transition locations, such as unsteady behavior or excessive up-wash. The root vortex system for all collective pitch angles was shown to slightly bloom above the surface, and the trailing tip vortex system seemed to lose stability as the collective pitch angle was increased. Tip vortices generated for a 4° collective pitch appear well-defined for the first few revolutions before they begin to lose stability; however, tip vortices for the 8° and 10° cases lose stability earlier on in the simulation. The distance between the tip vortices also increases as the collective pitch angle is increased which is due to the greater velocity generated with higher thrust. The wakes were also visualized by generating iso-surfaces of Q-criterion as shown in Figures 4.16-18. Similar trends in tip vortex stability described above were noticed. Additionally, the tip vortex system for the 10° study seemed to maintain stability to longer wake ages than the 8° case.

52
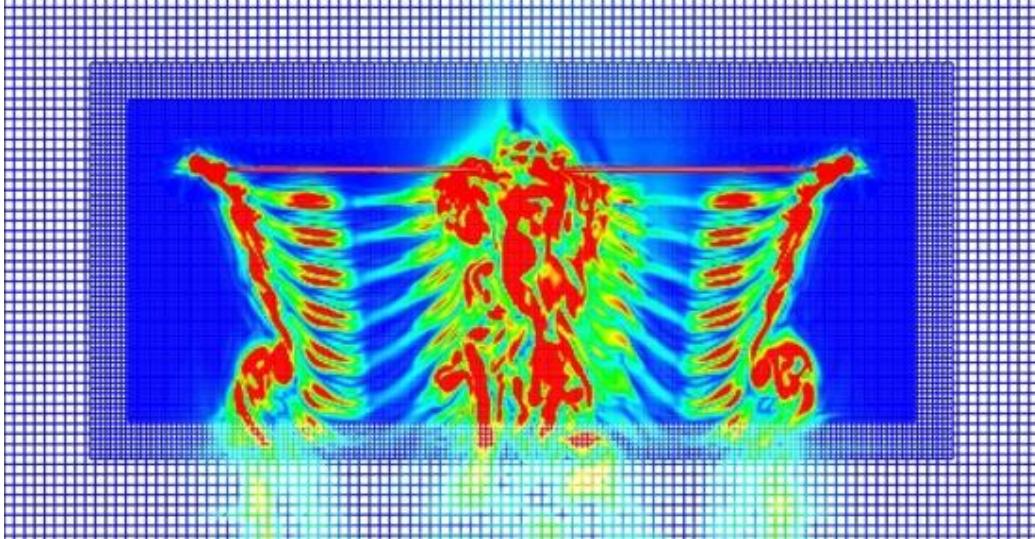
Figure 4.13 Vorticity magnitude contours for a 4° collective pitch.
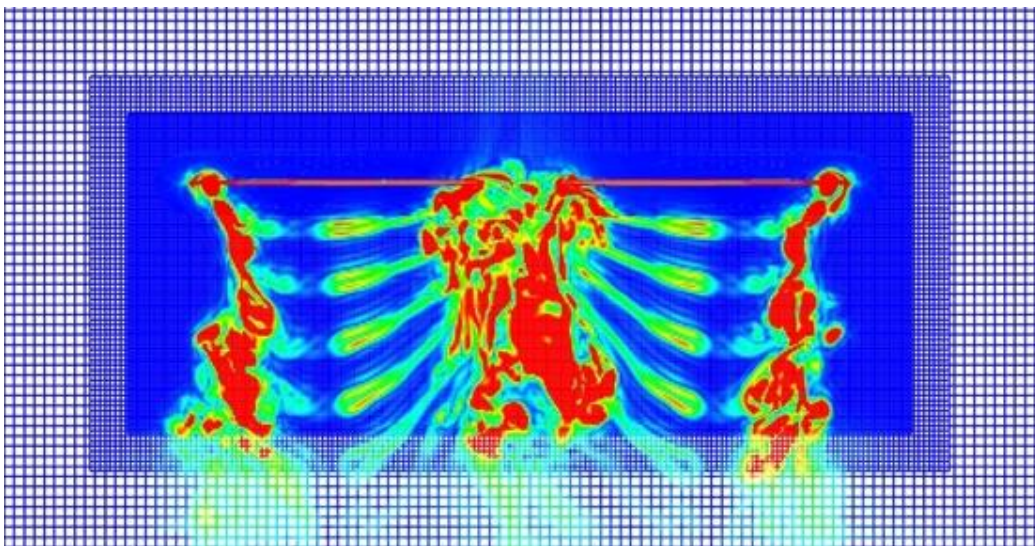
Figure 4.14 Vorticity magnitude contours for an 8° collective pitch.
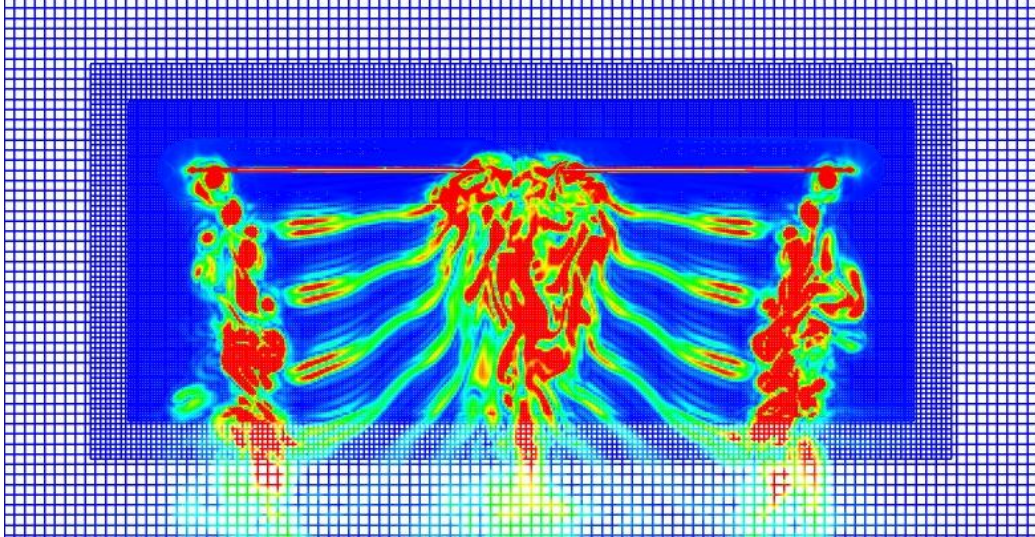
Figure 4.15 Vorticity magnitude contours for a 10° collective pitch.
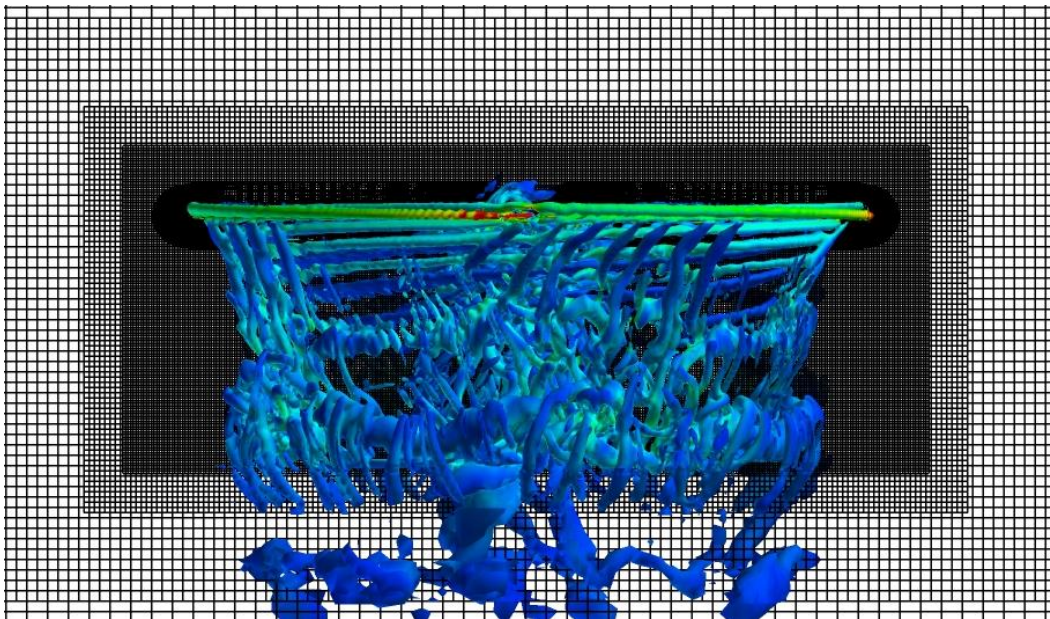
Figure 4.16 Iso-surfaces of Q-criterion = -0.0005 colored by vorticity magnitude for a 4° collective pitch.
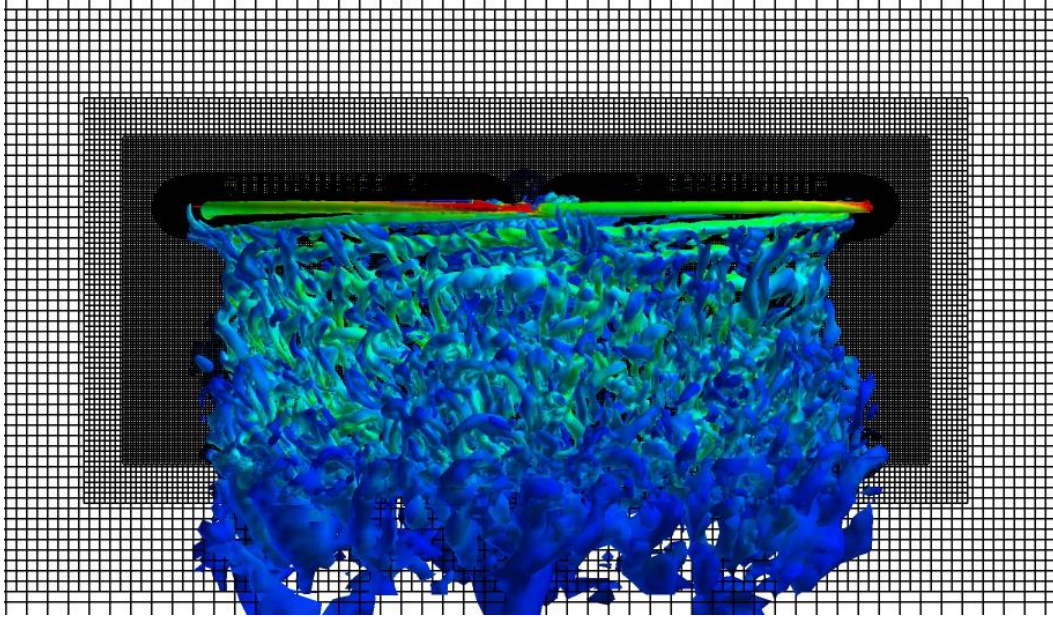
Figure 4.17 Iso-surfaces of Q-criterion = -0.0005 colored by vorticity magnitude for an 8° collective pitch.
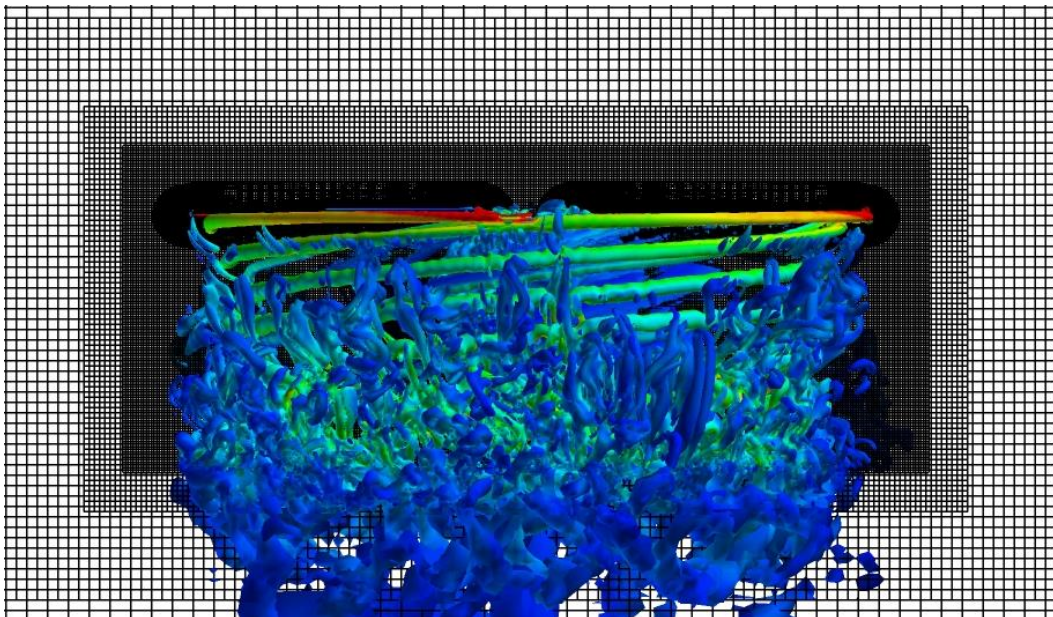
Figure 4.18 Iso-surfaces of Q-criterion = -0.0005 colored by vorticity magnitude for a 10° collective pitch.

Vorticity magnitude contours were captured for the first few revolutions to analyze the root and tip vortex system behavior for a 10° collective pitch as shown in Figure 4.19. The vorticity behavior was evaluated after 1 revolution, 3 revolutions, and 5 revolutions. After completing one revolution, the starting vortex is clearly visible at the tip. Additionally, an initial up-wash from the root vortex system is created as indicated by the upward advection of vorticity.

Upon completing 3 revolutions, the initial up-wash is much more significant which affects transition around the hub. The tip vortices seem to maintain their stability as the starting vortex travels downstream. With the completion of 5 revolutions, the up-wash created by the root vortex system moves closer to the rotor center as it propagates beneath the blade surface. The tip vortex system continues to maintain stability which follows the behavior noticed in Figure 4.15, but it is evident that the tip vortices lose their stability further downstream.
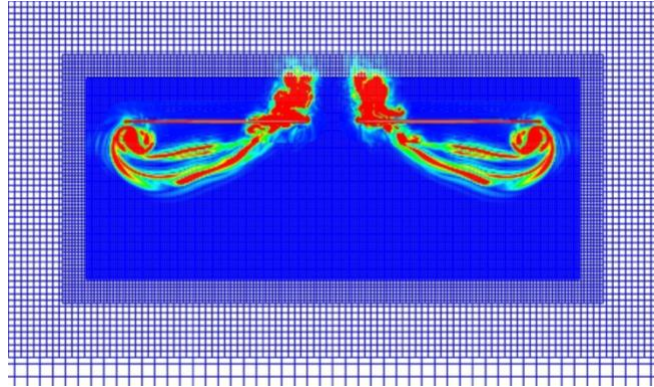
(a)
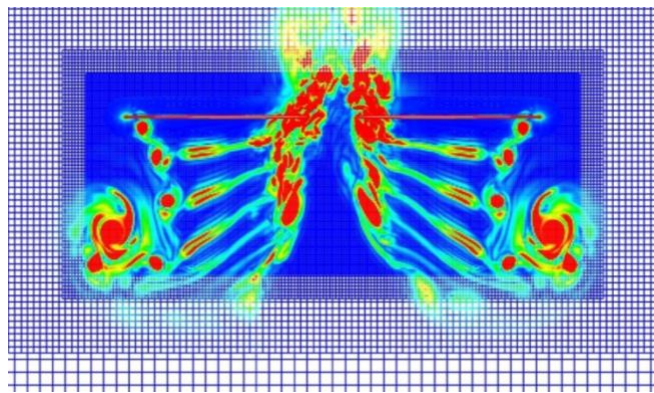
(b)
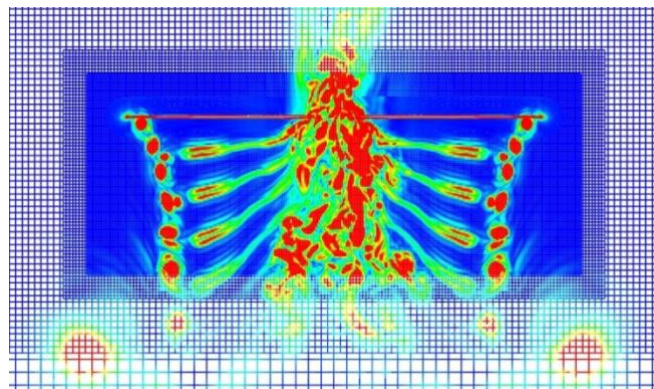
(c)

Figure 4.19 Startup vorticity magnitude contours for a 10° collective pitch at (a) 1 revolution, (b) 3 revolutions, and (c) 5 revolutions.

4.3 Rotor-Fuselage Interaction

Thrust and torque predictions for the rotor-fuselage configuration were compared to those of the isolated rotor to determine effects caused by the fuselage in terms of transition locations and rotor performance. Table 4.2 lists average values for thrust and torque and standard deviations at all collective pitch cases, and the results obtained represented the final revolution. All cases converged well, but the standard deviations are slightly larger than the isolated rotor cases. It was shown that thrust increased as the collective pitch angle increased, and the rotor-fuselage simulations achieved higher thrust values than the isolated rotor simulations as expected. Higher thrust values are obtained due to the effective up-wash created from the root vortex system as it interacts with the fuselage.

The average values calculated for figure of merit were compared with measured values obtained from wind tunnel tests described earlier [51]. The difference between the predicted and measured figure of merit for a collective pitch angle of 8° with the fuselage was roughly 0.32%, and the error between the predicted and measured figure of merit for a collective pitch angle of 10° was approximately 1.33%. The predictions obtained were significantly more accurate than results for the isolated rotor. As mentioned earlier, the measurements in the wind tunnel were made with the fuselage configuration.

Figures 4.20-22 present the unsteady thrust and torque behaviors against time step for the last two revolutions using the rotor-fuselage configuration at various collective pitch angles. Similar to the isolated rotor simulations, no significant improvement was noticeable by initializing the flow at a 1° of rotation per time step at a 4° collective pitch. The spikes in thrust and torque for the final two revolutions validate effects caused by up-wash as they occur twice during each revolution.

Table 4.2 Average Values of Rotor-Fuselage Hover Predictions.

Collective, θ	C_T/σ	C_Q/σ	FM
4°	0.0276 ∓ 0.00127	0.00200 ∓ 0.0000502	0.519 ∓ 0.0235
8°	0.0625 ∓ 0.00204	0.00487 ∓ 0.0000961	0.729 ∓ 0.0224
10°	0.0840 ∓ 0.00255	0.00724 ∓ 0.000101	0.764 ∓ 0.0255
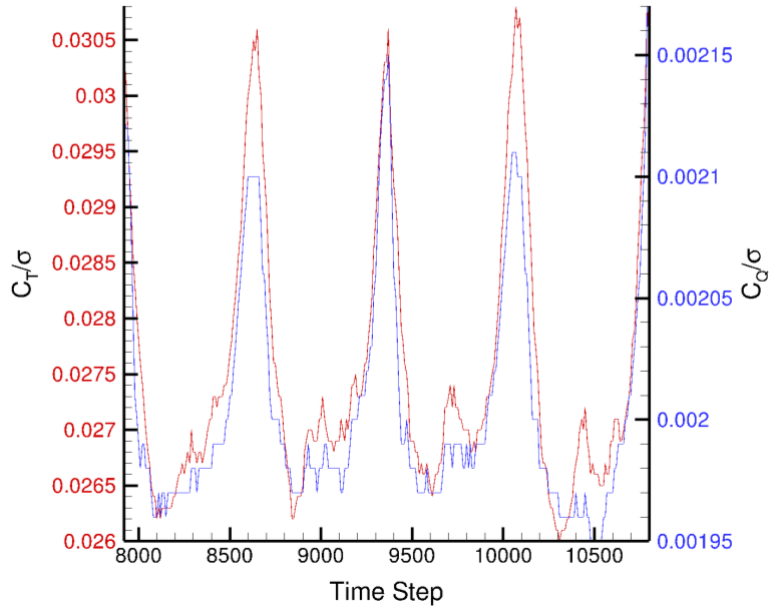
Figure 4.20 Thrust and torque convergence history for a 4° collective pitch.
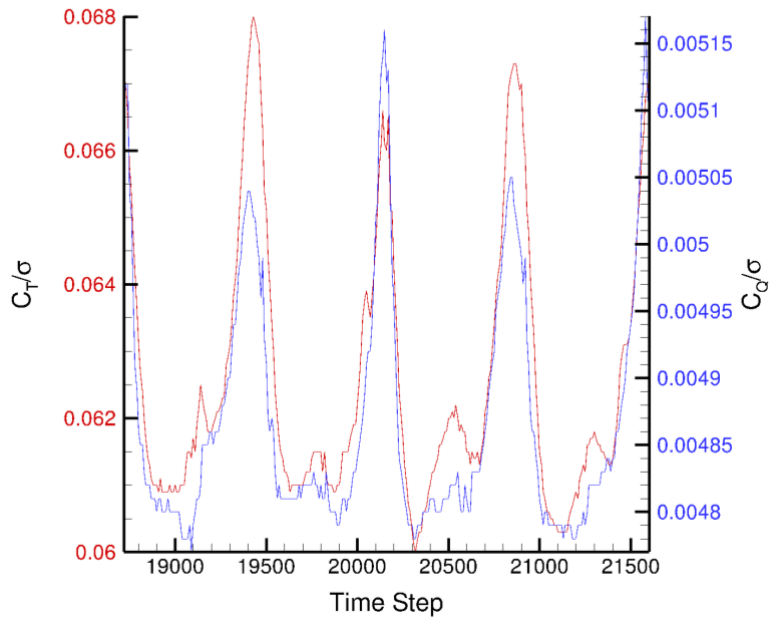
Figure 4.21 Thrust and torque convergence history for an 8° collective pitch.
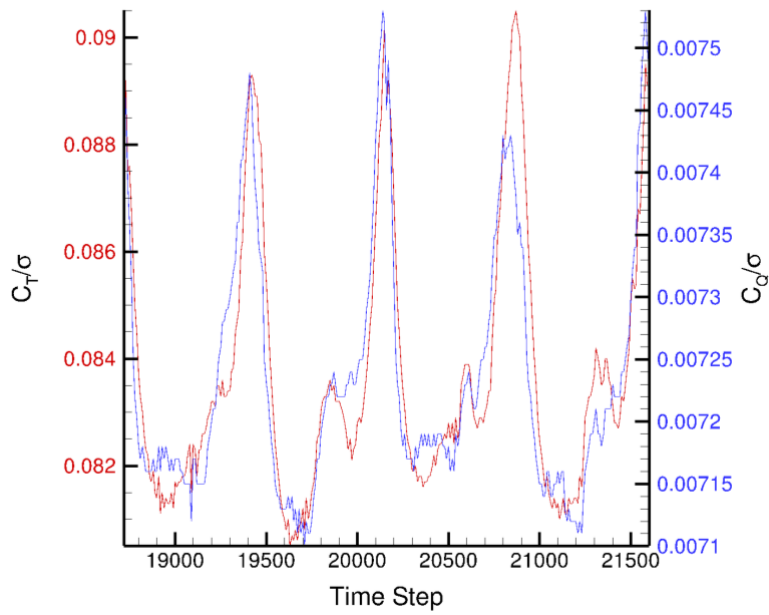
Figure 4.22 Thrust and torque convergence history for a 10° collective pitch.

Fuselage effects on wake structures for varying collective pitch angles are evident in iso-surfaces of Q-criterion colored by vorticity magnitude as shown in Figures 4.23-25. Similar to the isolated rotor simulations, the tip vortex system seemed to lose stability as the collective pitch angle was increased. The tip vortices for the 4° collective pitch case seem to lose coherence further downstream compared to the 8° collective pitch case where the tip vortices lose stability early on in the simulation. The tip vortices for the 10° collective pitch simulation are clearly visible, but the unsteady disturbances are much larger and more clustered than the other two runs. The tip vortices are partly affected by the fuselage tail as seen outside the tip vortices. The effective up-wash (more appropriately, a reduction in downwash) is much more significant in the rotor-fuselage simulations than in simulations involving the isolated rotor, and the effect grows stronger as the collective pitch angle increases. This also affects transition on the blade surfaces and the fuselage. The thrust increase is also represented by the distance between the tip vortices as the collective pitch is increased.
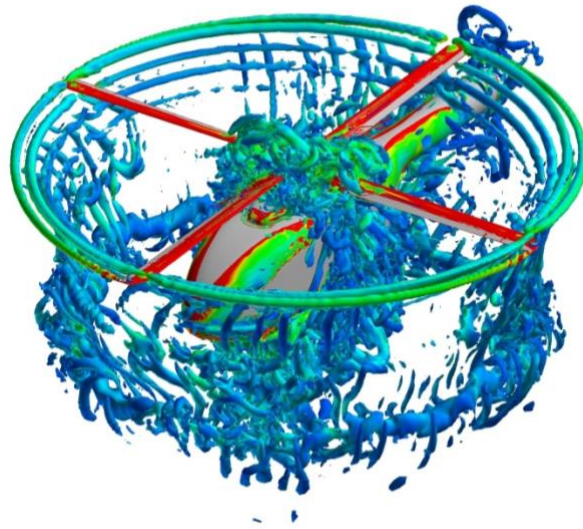
Figure 4.23 Iso-surfaces of Q-criterion = -0.001 colored by vorticity magnitude for a 4° collective pitch.
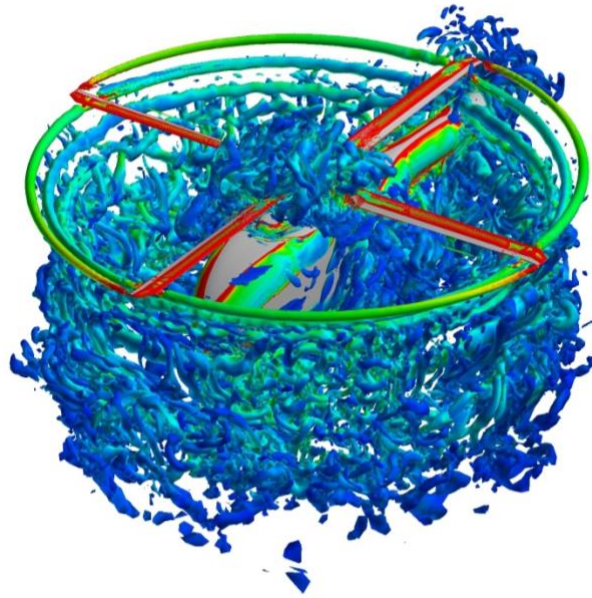
Figure 4.24 Iso-surfaces of Q-criterion = -0.001 colored by vorticity magnitude for an 8° collective pitch.
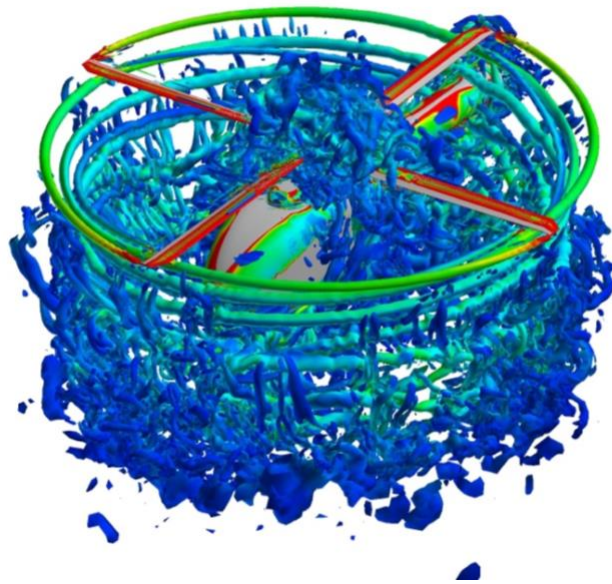
Figure 4.25 Iso-surfaces of Q-criterion = -0.001 colored by vorticity magnitude for a 10° collective pitch.

The predicted blade surface transition locations were analyzed using Spalart's Turbulence Index [32] as shown in Figures 4.26-28. These images also indicate transition locations on the fuselage. Top and isometric views were used to visualize the symmetry between the blade surface and fuselage transition. Additionally, the predictions for collective pitch angles of 8° and 10° were compared to measured [51] and predicted data from Jain [46].

Upper surface transition patterns for both collective pitches matched measured transition lines fairly well; however, the delayed transition patch observed for the 8° collective pitch isolated rotor case appeared in the rotor-fuselage simulations as well. As shown before, this behavior was also recognized by Jain [46]. It was noticed that the blades did not display symmetrical transition patterns for collective pitches of 8° and 10°. For the 4° collective pitch case, a trip in the flow was observed in the transition patterns due to the up-wash created from the root vortex and fuselage interaction. A slight difference in the transition pattern near the tip was noticed for the blade directly above the fuselage tail. The reaction seems to occur due to up-wash created from the root vortices interacting with the tail bloom. Also, due to the blade rotation, the transition patterns along the fuselage surface were not symmetrical.
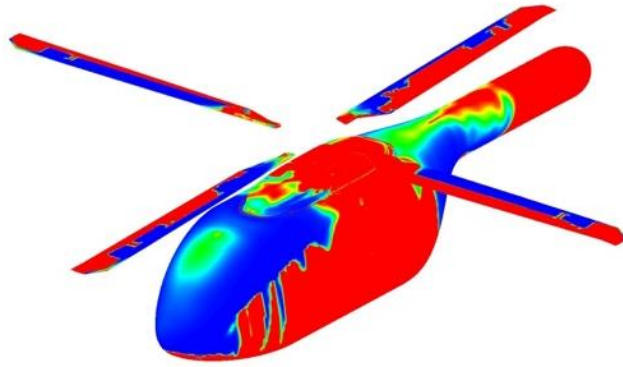
(a)
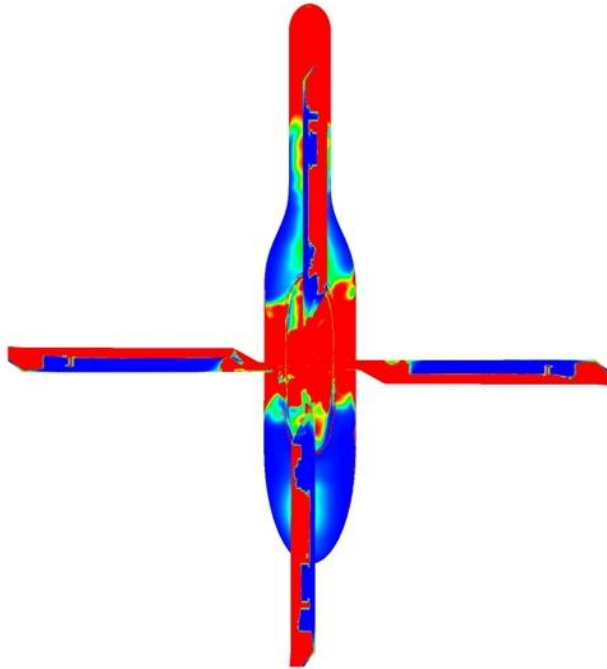
(b)

Figure 4.26 Spalart's Turbulence Index at a 4° collective pitch using an (a) isometric view and a (b) top view.
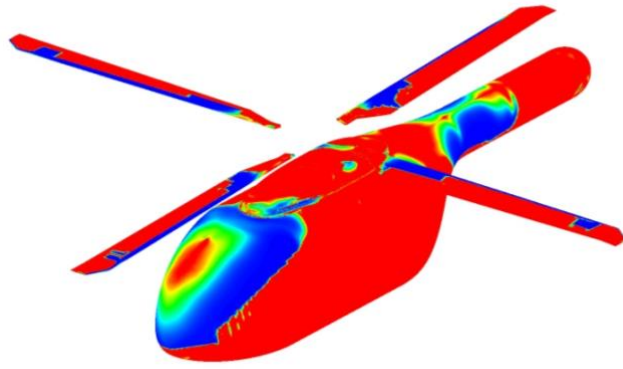
(a)
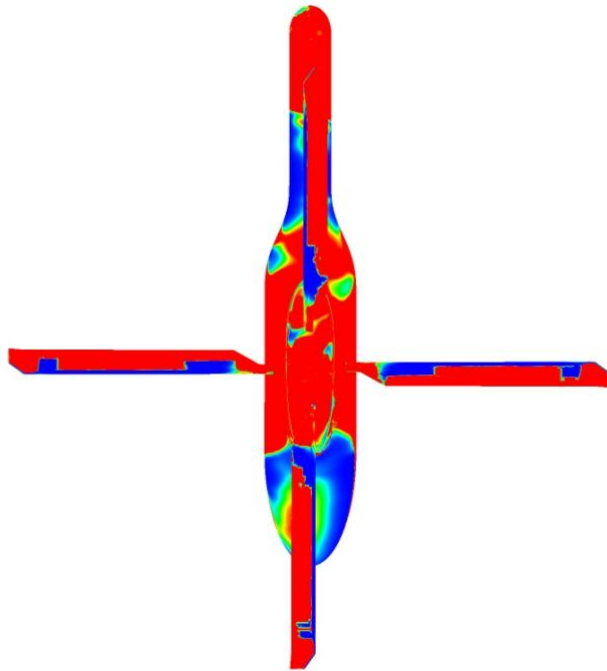
(b)

Figure 4.27 Spalart's Turbulence Index at an 8° collective pitch using an (a) isometric view and a (b) top view.
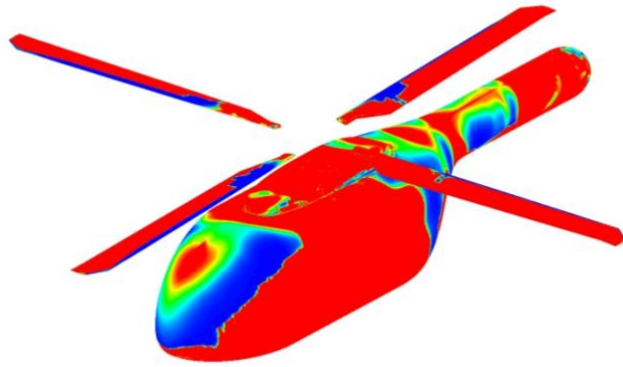
(a)
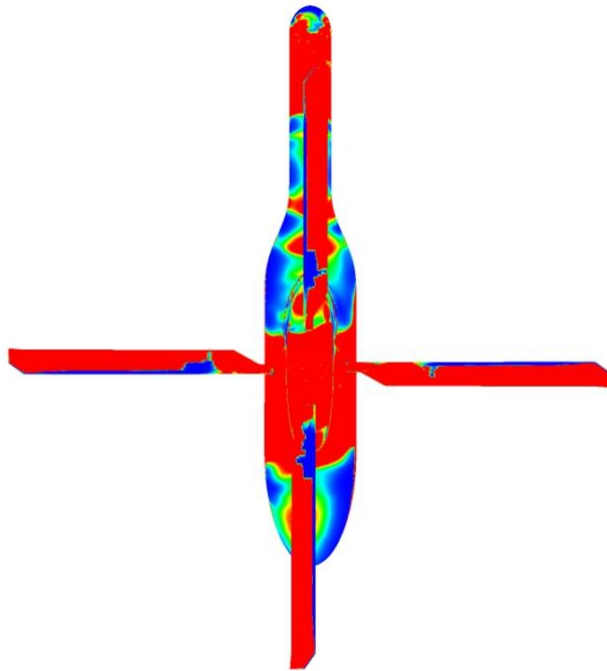
(b)

Figure 4.28 Spalart's Turbulence Index at a 10° collective pitch using an (a) isometric view and a (b) top view.

To explore the tip and root vortex stability with the rotor-fuselage configuration, vorticity magnitude contours centered in the y-plane were examined for the first 5 revolutions. The images were taken for a 10° collective pitch and at 1 revolution, 3 revolutions, and 5 revolutions as shown in Figure 4.29. The starting vortex is formed after 1 revolution, and the initial up-wash effect is generated from fuselage interactions. As mention earlier, the initial up-wash was much greater than in the isolated rotor results due to the blockage of the fuselage.

After completing 3 revolutions, it was clear that tip vortices were formed in front of the fuselage nose, but the flow from the root vortex curled around the body and mixed with the starting vortex and tip vortices near the fuselage tail. The first revolution near the fuselage tail was visible, and the remaining tip vortices were clustered with the root vortex. The root vortex up-wash was also still growing above the blade surface. Once 5 revolutions were reached, the starting vortex was clearly visible as were the tip vortices in front of the fuselage nose. The flow around the fuselage mixed with the tip vortices near the fuselage trail only grew more unstable, and the effective up-wash was still evident above the hub.
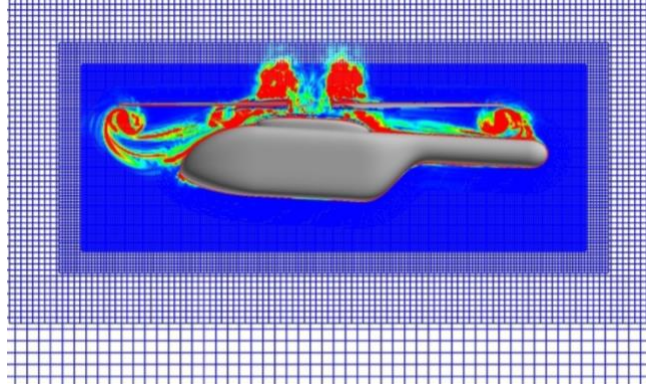
(a)
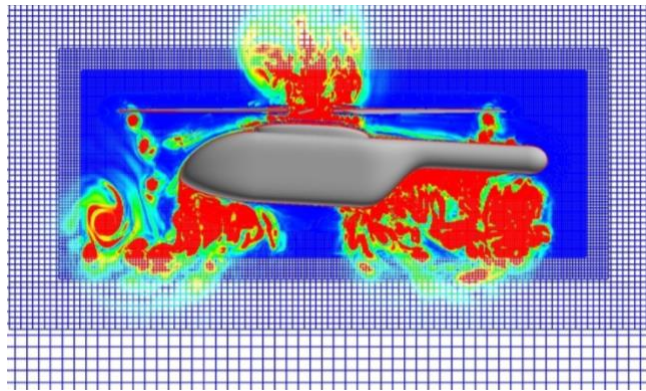
(b)
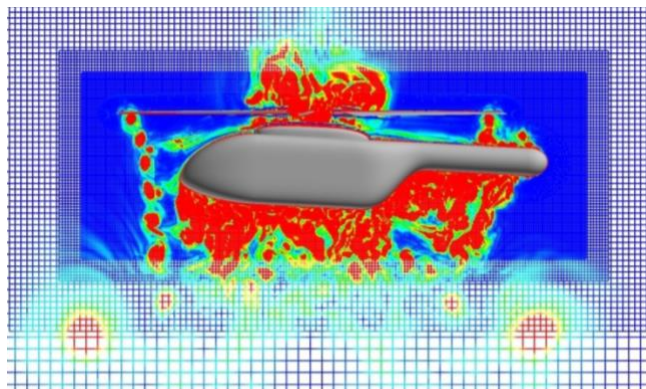
(c)

Figure 4.29 Vorticity magnitude contours for a 10° collective pitch upon completion of (a) 1 revolution, (b) 3 revolutions, and (c) 5 revolutions.

Figure of merit as it depends on thrust was assessed for the isolated rotor and rotor-fuselage simulations, and the predictions were compared to measured data as shown in Figure 4.30. The predicted results for both configurations agreed well with experimental data. The results obtained for the rotor-fuselage configuration displayed higher figure of merit values due to increased thrust. This feature was a result of the up-wash produced from the root vortex interaction with the fuselage hub showing the impact of including the fuselage in simulations.

With higher figure of merit values, rotor-fuselage predictions for collective pitch angles of 8° and 10° agreed better with experimental data than the isolated rotor simulations. An explanation for the improved agreement was the rotor-fuselage setup for the experimental tests conducted. Tests were not completed with the isolated rotor at the same conditions. Of all cases, the simulations conducted using a collective pitch of 8° matched the experimental results the closest. For both configurations at a collective pitch of 10°, results obtained underpredicted the measured data due to lower surface transition disagreements. The thrust values provided in the experimental data did not represent a 4° collective pitch. If the measured data trend was extended to lower thrust values, the predicted data acquired with both configurations would seem to slightly overpredict the measurements.

To further analyze the impact of the fuselage, chordwise pressure distributions were determined for each blade in both configurations as shown in Figures 4.31-34. The distributions were taken at roughly 75% of the rotor radius. The blade locations shown represented four azimuthal positions: 0° (aft blade), 90° (advancing side blade), 180° (front blade), and 270° (retreating side blade). The pressure differences where transition occurs are clearly shown for the front and aft blades which are directly above the fuselage. The pressure distributions for the advancing and retreating side blades do not experience any visible impact on pressure distribution due to their positioning. The aft blade experiences the largest impact due to tail bloom.
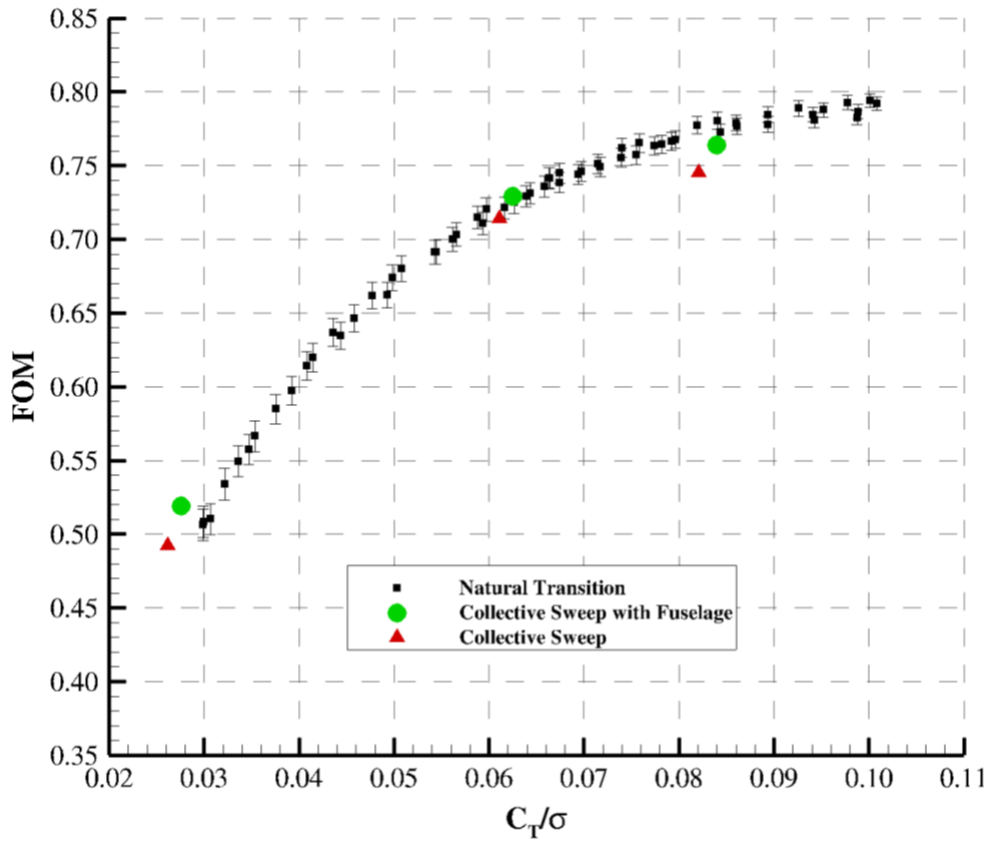
Figure 4.30 Rotor performance CFD and experimental comparison.
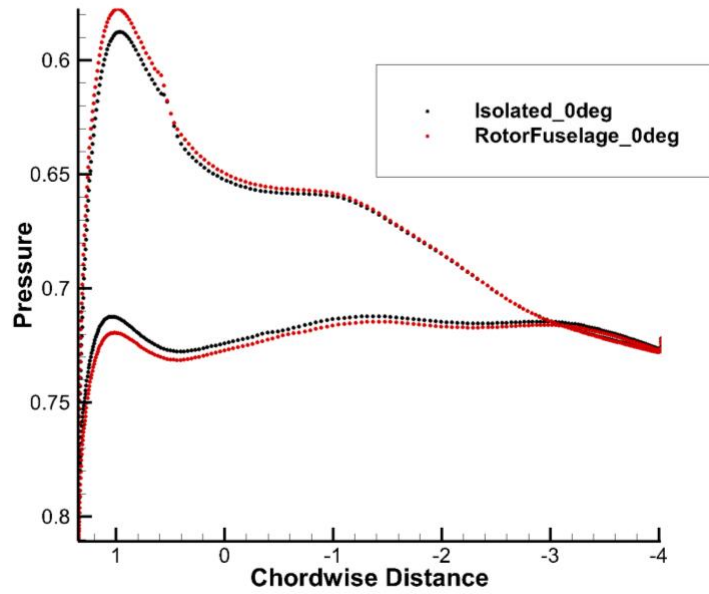
Figure 4.31 Chordwise pressure distribution for 10° collective pitch at aft position.
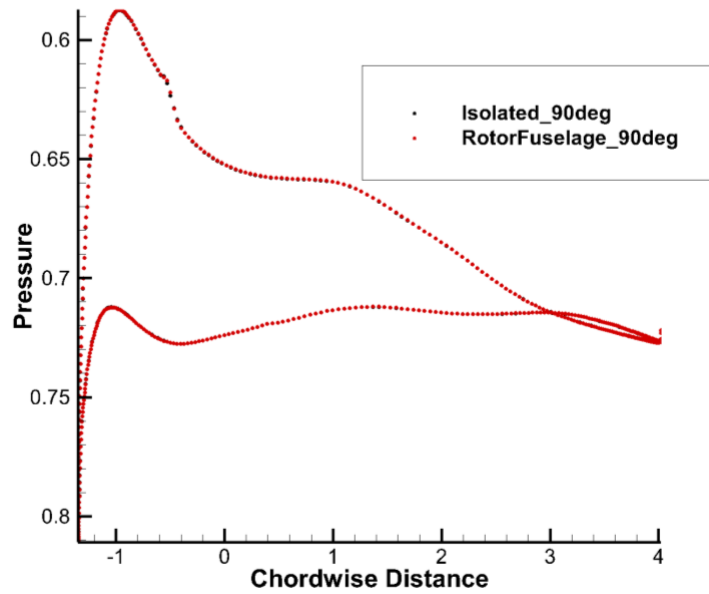
Figure 4.32 Chordwise pressure distribution for 10° collective pitch at advancing side position.
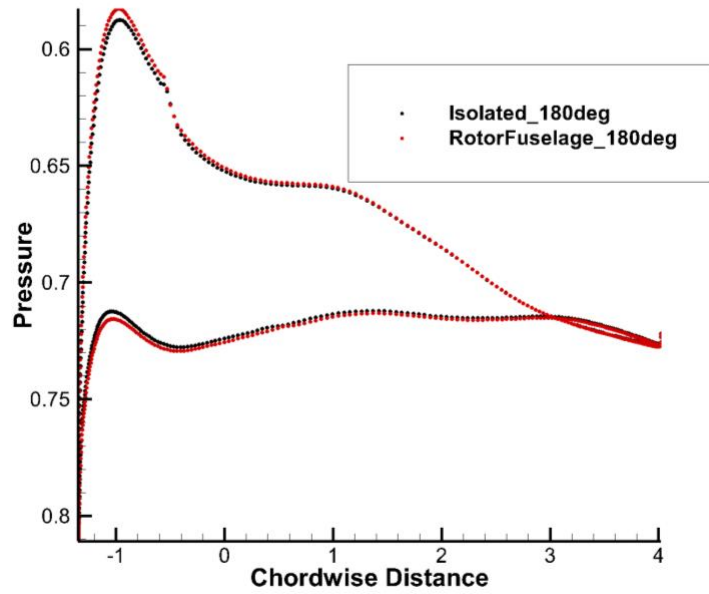
Figure 4.33 Chordwise pressure distribution for 10° collective pitch at front position.
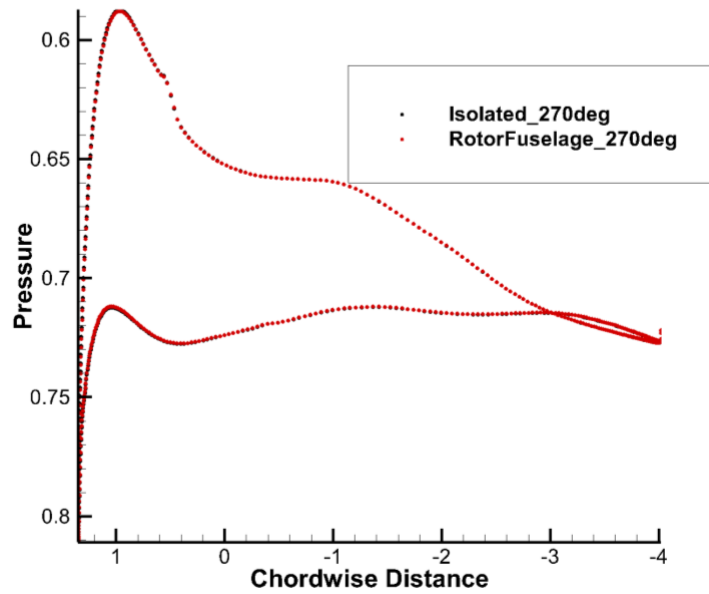
Figure 4.34 Chordwise pressure distribution for 10° collective pitch at retreating side position.

CHAPTER 5
CONCLUSIONS

Structured, overset RANS simulations were completed using the OVERFLOW 2.2 compressible flow solver to assess the effects of transition modeling and the impact of a fuselage in rotor simulations. The configurations used for the simulations were an isolated PSP rotor and a rotor-fuselage setup with a ROBIN Mod7 fuselage shell. The fuselage shell was added to explore the effects the body would have on the blade transition and wake vortex system. Additionally, the addition of the fuselage tested the abilities and limitations of the transition model used. The specific transition/turbulence model used for all simulations was the SA-neg-RC-AFT2017b in addition to DDES used to provide hybrid RANS/LES behavior.

Simulations for each configuration were divided into 3 cases using collective pitch angles of 4°, 8°, and 10°. The results were compared with measured data and CFD data obtained from previous studies. Simulations for both configurations reached convergence criteria and followed trends seen in measured rotor performance. Hover predictions with the isolated rotor at an 8° collective pitch in terms of figure of merit differed from experimental data by about 1.15%. Figure of merit calculations made for a 10° collective pitch, however, resulted in a difference of about 3.39% relative to experiment. Possible causes for the larger difference are still being explored; however, measured data are only available for the rotor-fuselage configuration. The predicted blade surface transition lines for the isolated rotor setup also lined up with measured transition locations. A slight difference due to a delayed transition patch further along the blade surface for an 8° collective pitch was noticed, and the lower blade surface shared a few differences in transition patterns due to the unsteady behavior of the root vortex system. It was observed that the root vortex and tip vortices became more unstable as the collective pitch angle was increased, and the distance between tip vortices grew as collective pitch was increased demonstrating the increase in thrust at higher collective pitches. While analyzing the first

73

5 revolutions at a 10° collective pitch, the tip vortices maintained coherence meaning that the stability was lost further downstream. Also, for the isolated rotor case, there is an initial up-wash from the root vortex system within the first 5 revolutions. The up-wash seems to slowly weaken after 3 revolutions.

Figure of merit predictions for the rotor-fuselage configuration at an 8° collective pitch differed from experimental results by roughly 0.32%, and the predictions at a 10° collective pitch displayed a difference of approximately 1.33%. This proved that the rotor-fuselage configuration was able to provide more accurate predictions than the isolated rotor due to the increased thrust generated by up-wash. The wake structures generated revealed that the root vortex was significantly more unstable due to the fuselage lying beneath the blades, and the tip vortices were slightly affected by the fuselage tail extending past the blades. The unsteady behavior shown in the root and tip vortices grew as collective pitch was increased, and up-wash produced from the root vortex interacting with the fuselage shell became more prominent. This affected the transition patterns on the blade surface near the hub. The blade transition patterns were able to match measured transition locations as well as transition lines seen by the isolated rotor. It was also noticed that the blades did not exhibit rotational symmetry in the transition lines. The blade directly above the fuselage tail was slightly different near the tip region due to up-wash, and a trip in the flow due to up-wash was noticed in the transition lines at a 4° collective pitch. The first 5 revolutions were once again studied at a 10° collective pitch to explore the tip and root vortex systems due to their unsteady behavior. The tip vortices seemed to lose stability due to interactions with the root vortex. Additionally, the root vortex up-wash grew as well as the downwash disturbances under the fuselage as more revolutions were completed.

To further analyze transition modeling capabilities, it is essential to study the transition patterns near the tip closely. Also, it is of interest to test the transition model used in a forward flight simulation with both configurations. Possible causes for unsteady tip vortex behavior are being assessed, and a possible solution may be averaging the entire data set at one collective pitch rather than analyzing transition at the final point in the simulation. Rotor performance for both configurations at a 10° collective pitch require

evaluation to determine causes for significant underpredictions of measured data. The completed studies showed the importance in including the fuselage in rotor simulations due to the significant impact on hover performance, transition predictions, and pressure distribution predictions.

LIST OF REFERENCES

1. Leishman, G. J., *Principles of Helicopter Aerodynamics*, 2nd ed., Cambridge University Press, New York, 2006, Chaps. 1-3.

2. Harding, S., "Sikorsky H-60 Black Hawk," U.S. Army Aircraft Since 1947, Schiffer Publishing Ltd., Atglen, Pennsylvania, 1997, ISBN 0-7643-0190-X.

3. Eden, P., "Sikorsky H-60 Black Hawk/Seahawk," Encyclopedia of Modern Military Aircraft, Amber Books, 2004, ISBN 1-904687-84-9.

4. Jackson, P., "Sikorsky BLACK HAWK Helicopter," *Lockheed Martin*, www.lockheedmartin.com/en-us/products/sikorsky-black-hawk-helicopter.html.

5. "Bell Helicopter Introduces the Bell 412EPI: Boosts Performance and Reliability," (Press release). *Textron*, Las Vegas, N, 4 March 2013. Retrieved 11 March 2016.

6. Roelofs, E., "Italy's Flying Foresters," *Air International* Vol. 82, No. 4, pp. 78–81, ISSN 0306-5634.

7. Haynes, M. L. and Young, C. M., ed. "Department of the Army Historical Summary, FY 1987, Chapter 5: Modernizing and Equipping the Army," Center of Military History, United States Army, 1995.

8. Nichols, L., "Boeing: Historical Snapshot: B-29 Superfortress," Boeing, www.boeing.com/defense/ah-64-apache/.

9. "Northrop lifts Navy to new era for unmanned flight," Aerotech News and Review, 22 December 2006.

10. "RQ-8B," *Military Factory*, February 25, 2013. Accessed July 20, 2018.

11. McCroskey, W. J., "Vortex Wakes of Aircraft," *33rd AIAA Aerospace Sciences Meeting*, AIAA Paper 95-0530, Reno, NV, January 1995.

12. Leishman, J. G. and Bagai, A., "Challenges in Understanding the Vortex Dynamics of Helicopter Rotor Wakes," *AIAA Journal*, Vol. 36, No. 7, 1998, pp. 1130-1140.

13. Hariharan, N. and Sankar, L. N., "A Review of Computational Techniques for Rotor Wake Modeling," *38th AIAA Aerospace Sciences Meeting*, AIAA Paper 00-0114, Reno, NV, January 2000.

14. Hariharan, N., Egolf, A., and Sankar, L. N., "Simulation of Rotor in Hover: Current State and Challenges," *52nd AIAA Aerospace Sciences Meeting*, AIAA Paper 2014-0041, National Harbor, MD, January 2014.

15. Shenoy, R., Smith, M. J., and Park, M. A., "Unstructured Overset Mesh Adaptation with Turbulence Modeling for Unsteady Aerodynamic Interactions," *Journal of Aircraft*, Vol. 51, No. 1, 2014, pp. 161-174.

16. Smith, M. J., Jacobson, K. E., Grubb, A. L., Wachspress, D. A., and Whitehouse, G. R., "Evaluation of Rotor Hover Performance With Differing Blade Tip Shapes Using A Carefree Hybrid Methodology," *53rd AIAA Aerospace Sciences Meeting*, AIAA Paper 2015-1713, Kissimmee, FL, January 2015.

17. Baeder, J. D., Medida, S., and Kalra, T. S., "OVERTURNS Simulations of S-76 Rotor in Hover," *52nd AIAA Aerospace Sciences Meeting*, AIAA Paper 2014-0045, National Harbor, MD, January 2014.

18. Jung, Y. S., Govindarajan, B., and Baeder, J. D., "Unstructured/Structured Overset Methods for Flow Solver Using Hamiltonian Paths and Strand Grids," *54th AIAA Aerospace Sciences Meeting*, AIAA Paper 2016-1056, San Diego, CA, January 2016.

19. Kalra, T. S. and Baeder, J. D., "Modeling Subscale Rotor Wake in Ground Effect with Accurate Turbulent Length Scales," *AIAA Journal*, Vol. 55, No. 9, 2017, pp. 3085-3094.

20. Barakos, G.N. and Jimenez-Garcia A., "Hover Predictions of the S-76 Rotor using HMB2 - Model to Full-Scale," *54th AIAA Aerospace Sciences Meeting*, AIAA Paper 2016-0299, San Diego, CA, January 2016.

21. Yoon, S., Pulliam T.H., and Chaderjian N.M., "Simulations of XV-15 rotor flows in hover using OVERFLOW," *5th Decennial AHS Aeromechanics Specialists' Conference*, San Francisco, CA, January 2014.

22. Yoon, S., Chaderjian, N., Pulliam, T. H., and Holst, T., "Effect of Turbulence Modeling on Hovering Rotor Flows," *45th AIAA Fluid Dynamics Conference*, AIAA Paper 2015-2766, Dallas, TX, June 2015.

23. Jain, R., "A Comparison of CFD Hover Predictions for the Sikorsky S-76 Rotor," *54th AIAA Aerospace Sciences Meeting*, AIAA Paper 2016-0032, San Diego, CA, January 2016.

24. Jain, R., "Effect of Facility Walls and Blade Aeroelasticity on PSP Rotor Hover Performance Predictions," *56th AIAA Aerospace Sciences Meeting*, AIAA Paper 2018-0305, Kissimmee, FL, January 2018.

25. Abras, J. and Hariharan N.S., "Comparison of CFD Hover Predictions on the S-76 Rotor," *53rd AIAA Aerospace Sciences Meeting*, AIAA Paper 2015-1711, Kissimmee, FL, January 2015.

26. Abras, J. and Hariharan N.S., "Performance Impact of Tip Shape Variations on the S-76 Rotor Using kCFD," *54th AIAA Aerospace Sciences Meeting*, AIAA Paper 2016-0298, San Diego, CA, January 2016.

27. Coder, J. G., "OVERFLOW Rotor Hover Simulations Using Advanced Turbulence and Transition Modeling," *55th AIAA Aerospace Sciences Meeting*, AIAA Paper 2017-1431, Grapevine, TX, January 2017.

28. Coder, J. G. and Maughmer, M. D., "Computational Fluid Dynamics Compatible Transition Modeling Using an Amplification Factor Transport Equation," *AIAA Journal*, Vol. 52, No. 11, 2014, pp. 2506-2512.

29. Menter, F. R., Smirnov, P. E., Liu, T., and Avancha, R. "A one-equation local correlation-based transition model," *Flow, Turbulence and Combustion*, Vol. 95, No. 4, 2015, pp. 583-619.

30. Langtry, R. B. and Menter, F. R., "Correlation-Based Transition Modeling for Unstructured Parallelized Computational Fluid Dynamics Codes," *AIAA Journal*, Vol. 47, No. 12, 2009, pp. 2894-2906.

31. Medida S. and Baeder, J.D., "Application of the Correlation-based -Ret Transition Model to the Spalart-Allmaras Turbulence Model," *20th AIAA Computaional Fluid Dynamics Conference*, AIAA Paper 2011-3979, Honolulu, HI, June 2011.

32. Spalart, P. R. and Allmaras, S. R., "A One-Equation Turbulence Model for Aerodynamic Flows," *Recherche Aerospatiale*, No. 1, 1994, pp. 5-21.

33. Menter, F. R., "Two-Equation Eddy-Viscosity Turbulence Models for Engineering Applications," *AIAA Journal*, Vol. 32, Aug. 1994, pp. 1598-1605.

34. Menter, F. R., "Zonal Two Equation k-ω Turbulence Models for Aerodynamic Flows," *23rd AIAA Fluid Dynamics, Plasma Dynamics, and Lasers Conference*, AIAA Paper 93-2906, Orlando, Florida, July 1993.

35. Baldwin, B.S. and Barth, T.J., "A One-Equation Turbulence Transport Model for High Reynolds Number Wall-Bounded Flows," *29th AIAA Aerospace Sciences Meeting*, AIAA Paper 91-0610, Reno, NV, January 1991.

36. Wilcox, D.C., TURBULENCE MODELING FOR CFD, 3rd ed., DCW Industries, Inc., La Canada, CA, 2006.

37. Baldwin, B.S. and Lomax, H., "Thin Layer Approximation and Algebraic Model for Separated Turbulent Flows," *16th AIAA Aerospace Sciences Meeting* AIAA Paper 78-0257, Huntsville, AL, January 1978.

38. Hodara, J. and Simth, M. J., "Hybrid Reynolds-Averaged Navier–Stokes/Large-Eddy Simulation Closure for Separated Transitional Flows," *AIAA Journal*, Vol. 55, No. 6, 2017, pp. 1948-1958.

39. Jimenez Garcia, A. and Barakos G.N., "Hover Performance Predictions on the S-76 Rotor uisng HMB2," *53rd AIAA Aerospace Sciences Meeting*, AIAA Paper 2015-1712, Kissimmee, FL, January 2015.

40. Garcia, A. J., Colonia, S., Barakos, G.N., "Accurate Predictions of Hovering Rotor Flows Using CFD," *55th AIAA Aerospace Sciences Meeting*, AIAA Paper 2017-1666, Grapevine, TX, January 2017.

41. Sheng, C., Zhao, Q., and Wang, J., "S-76 Rotor Hover Prediction Using U^2NCLE Solver," *52nd AIAA Aerospace Sciences Meeting*, AIAA Paper 2014- 0044, National Harbor, MD, January 2014.

42. Sheng, C., Wang, J., and Zhao, Q., "S-76 Rotor Hover Predictions Using Advanced Turbulence Models," *53rd AIAA Aerospace Sciences Meeting*, AIAA Paper 2015-1715, Kissimmee, FL, January 2015.

43. Sheng, C., Zhao Q., and Hill M., "Investigations of XV-15 Rotor Hover Performance and Flow Field Using U^2NCLE and HELIOS Codes," *54th AIAA Aerospace Sciences Meeting*, AIAA Paper 2016-0303, San Diego, CA, January 2016.

44. Jain, R.K. and Potsdam M.A., "Hover Predictions on the Sikorsky S-76 Rotor using Helios," *52nd AIAA Aerospace Sciences Meeting*, AIAA Paper 2014-0207, National Harbor, MD, January 2014.

45. Jain, R., "Hover Predictions for the S-76 Rotor with Tip Shape Variation using CREATE-AV Helios," *53rd AIAA Aerospace Sciences Meeting*, AIAA Paper 2015-1244, Kissimmee, FL, January 2015.

46. Jain, R., "CFD Performance and Turbulence Transition Predictions on an Installed Model-Scale Rotor in Hover," *55th AIAA Aerospace Sciences Meeting*, AIAA Paper 2017- 1871, Grapevine, TX, January 2017.

47. Vieira, B. A. O., Kinzel, M. P., and Maughmer, M. D., "CFD Hover Predictions Including Boundary-Layer Transition," *55th AIAA Aerospace Sciences Meeting*, AIAA Paper 2017-1665, Grapevine, TX, January 2017.

48. Reed, H. L., Haynes T. S., and Saric, W. S., "Computational Fluid Dynamics Validation Issues in Transition Modeling," *AIAA Journal*, Vol. 36, No. 5, 1998, pp. 742-751.

49. Balch, D. T. and Lombardi, J., "Experimental Study of Main Rotor Tip Geometry and Tail Rotor Interactions," NASA Contractor Report 177336, February 1985.

50. Wadcock, A. J., Yamauchi, G. K., and Driver, D. M., "Skin Friction Measurements on a Hovering Full-Scale Tilt Rotor" *Journal of the American Helicopter Society*, Vol. 44, No. 4, 1999, pp. 312-319.

51. Overmeyer, A. D. and Martin, P. B., "Measured Boundary Layer Transition and Rotor Hover Performance at Model Scale," *55th AIAA Aerospace Sciences Meeting*, AIAA Paper 2017-1872, Grapevine, TX, January 2017.

52. Pressure Sensitive Paint Rotor Blade Definition Document, AIAA 4th Hover Special Sessions at SciTech 2017.

53. Schaeffler, N. W., Allan, B. G., Lienard, C., and Le Pape, A., "Progress Towards Fuselage Drag Reduction via Active Flow Control: A Combined CFD and Experimental Effort," *36th European Rotorcraft Forum*, Paper 064, Paris, France, September 2010.

54. Glauert, H. "Airplane Propellers" *Aerodynamic theory*, Springer, Berlin, Heidelberg, 1935, pp. 169-360.

55. Sørensen, J. N. "Blade-Element/Momentum Theory," *General Momentum Theory for Horizontal Axis Wind Turbines*, Springer, Cham, 2016, pp. 99-121.

56. Wissink, A. M., Sitaraman, J., Jayaraman B., Roget, B., Lakshminarayan, V. K., Potsdam M., Jain R., Bauer, A., and Strawn, R., "Recent Advancements in the Helios Rotorcraft Simulation Code," *54th AIAA Aerospace Sciences Meeting*, AIAA Paper 2016-0563, San Diego, CA, January 2016.

57. Steger, J. L., and Benek, J. A., "On the use of Composite Grid Schemes in Computational Aerodynamics," *Computer Methods in Applied Mechanics and Engineering*, Vol. 64, No. 1, 1987, pp. 301–320.

58. Meakin, R. L., Wissink, A. M., Chan, W. M., Pandya, S. A., Sitaraman, J., "On Strand Grids for Complex Flows," *18th AIAA Computational Fluid Dynamic Conference*, AIAA Paper 2007-3834, Miami, FL, June 2007.

59. Noack, R. W., "DiRTlib: A Library to Add an Overset Capability to Your Flow Solver," *17th AIAA Computational Fluid Dynamic Conference*, AIAA Paper 2005-5116, Toronto, Ontario, Canada, June 2005.

60. Sitaraman, M. F., Wissink, A., and Potsdam, M., "Parallel domain connectivity algorithm for unsteady flow computations using overlapping and adaptive grids," *Journal of Computational Physics*, 229(12):4703–4723, 2010.

61. Chan, W. M., Rogers, S. E., Pandya, S. A., Kao, D. L., Buning, P. G., Meakin, R. L., Boger, D. A., and Nash, S. M., "Chimera Grid Tools User's Manual, Version 2.1," Moffett Field, CA, 2010.

62. Spalart, P. R., "Detached-Eddy Simulation," *Annual Review of Fluid Mechanics*, Vol. 41, 2009, pp. 181-202.

63. Spalart, P. R., Deck, S., Shur, M. L., Squires, K. D., Strelets, M. Kh., and Travin, A., "A New Version of Detached-Eddy Simulation, Resistant to Ambiguous Grid Densities," *Theoretical and Computational Fluid Dynamics*, Vol. 20, No. 3, 2006, pp. 181-195.

64. Shur, M. L., Strelets, M. K., Travin, A. K., and Spalart, P. R., "Turbulence Modeling in Rotating and Curved Channels: Assessing the Spalart-Shur Correction," *AIAA Journal*, Vol. 38, No. 5, 2000, pp. 784-792.

65. Nichols, R. H. and Buning, P. G., "User's Manual for OVERFLOW 2.2," NASA Langley Research Center, Hampton, VA, Aug. 2010.

66. Wachspress, D., Quackenbush, T., and Boschitsch, A., "Rotorcraft Interactional Aerodynamics with Fast Vortex/Fast Panel Methods," *Journal of the American Helicopter Society*, Vol. 48, No. 4, 2003.

67. Srinivasan, G. R. and Baeder J. D., "TURNS: A Free-wake Euler/ Navier-Stokes Numerical Method for Helicopter Rotors," *AIAA Journal*, Vol. 31, No. 5, 1993, pp. 959-962.

68. Lawson, S. J., Steijl, R., Woodgate, M., and Barakos, G. N., "High performance computing for challenging problems in computational fluid dynamics," *Progress in Aerospace Sciences*, Vol. 52, No. 1, 2012, pp. 19–29.

69. Steijl, R. and Barakos, G. N., "Sliding mesh algorithm for CFD analysis of helicopter rotor-fuselage aerodynamics," *International Journal for Numerical Methods in Fluids*, Vol. 58, No. 5, 2008, pp. 527–549.

70. Steijl, R., Barakos, G. N., and Badcock, K., "A framework for CFD analysis of helicopter rotors in hover and forward flight," *International Journal for Numerical Methods in Fluids*, Vol. 51, No. 8, 2006, pp. 819–847.

71. Sheng, C. and Narramore, J., "Computational Simulation and Analysis of Bell Boeing Quad Tiltrotor Aero Interaction," *Journal of the American Helicopter Society*, Vol. 27, No. 4, 2009, pp 1-15.

72. Biedron, R. T., Carlson, J., Derlaga, J.M., Gnoffo, P.A., Hammond, D.P., Jones, W.T., Kleb B., Lee- Rausch, E.M., Nielsen E.J., Park, M.A., Rumsey, C.L., Thomas, J.L., and Wood, W.A., "FUN3D Manual: 12.7," NASA TM-2015-218761, May 2015.

73. Menter, F. R. and Egorov, Y., "The Scale-Adaptive Simulation Method for Unsteady Turbulent Flow Predictions, Part 1: Theory and Model Description," *Flow Turbulence and Combustion*, Vol. 85, 2010, pp. 113-138.

74. Parwani, A. A. and Coder, J. G., "Effect of Laminar- Turbulent Transition Modeling on PSP Rotor Hover Predictions," *56th AIAA Aerospace Sciences Meeting*, AIAA Paper 2018-0308, Kissimmee, FL, January 2018.

75. Parwani, A. A. and Coder, J. G., "CFD Predictions of Rotor-Fuselage Interactions Using Laminar-Turbulent Transition Modeling," *American Helicopter Society 74th Annual Forum*, Phoenix, AZ, May 2018.

76. Overmeyer, A. D. and Martin, P. B., "The Effect of Laminar Flow on Rotor Hover Performance," *American Helicopter Society 73rd Annual Forum*, Fort Worth, TX, May 2017.

77. Pulliam, T. H. and Steger, J. L., "Implicit finite-difference simulations of three-dimensional compressible flow," *AIAA Journal*, Vol. 18, No. 2, 1980, pp. 159-167.

78. "Pointwise V18.0," Pointwise Inc., Fort Worth, TX, 2018.

79. Roe, P. L., "Approximate Riemann solvers, parameter vectors, and difference schemes," *Journal of Computational Physics*, vol. 43, 1981, pp. 357-72.

80. Nichols, R. H., Tramel, R. W., and Buning, P. G., "Evaluation of Two High-Order Weighted Essentially Nonoscillatory Schemes," *AIAA Journal*, Vol. 46, No. 12, 2008, pp. 3090-3102.

81. Klopfer, G. H., Van der Wijngaart, R. F., Hung, C. M., and Onufer, J. T., "A Diagonalized Diagonal Dominant Alternating Direction Implicit (D3ADI) Scheme and Subiteration Correction," 29th AIAA Fluid Dynamics Conference, AIAA Paper 1998-2824, Albuquerque, NM, June 1998.

82. Henrick, A. K., Aslam, T. D., and Powers, J. M., "Mapped weighted essentially non-oscillatory schemes: achieving optimal order near critical points," *Journal of Computational Physics*, Vol. 207, No. 2, 2005, pp. 542-567.

83. Merriman, B. "Understanding the Shu–Osher conservative finite difference form," *Journal of Scientific Computing*, Vol. 19, No. 1-3, 2003, pp. 309-322.

84. Bardina, J. and Lombard, C . K ., "Three Dimensional Hypersonic Flow Simulations with the CSCM Implicit Upwind Navier-Stokes Method," AIAA Paper No. 87-1114, 1987.

85. Pulliam, T. H. and D. Chaussee, "A diagonal form of an im- plicit approximate-factorization algorithm," *Journal of Computational Physics*, Vol. 39, No. 2, 1981, pp. 347–363.

86. Allmaras, S. R., Johnson, F. T., and Spalart, P. R., "Modifications and Clarifications for the Implementation of the Spalart-Allmaras Turbulence Model," *7th International Conference on Computational Fluid Dynamics*, ICCFD7-1902, Big Island, HI, July 2012.

87. Drela, M. and Giles, M. B. "Viscous-inviscid analysis of transonic and low Reynolds number airfoils," *AIAA Journal*, Vol. 25, No. 10, 1987, pp. 1347-1355.

88. Mack, L. M., "Transition and Laminar Instability," NASA CR-153203, 1977.

89. Drela, M., "MISES Implementation of Modified Abu-Ghannam/Shaw Transition Criterion (Second Revision)", Massachusetts Institute of Technology Dept. of Aeronautics and Astronautics, July 1998.

VITA

Ashwin Ashok Parwani was born in Sevierville, TN and raised in Gatlinburg, TN to the parents of Ashok and Nita Parwani. He attended Gatlinburg-Pittman High School and selected to pursue a Bachelor of Science degree in Aerospace engineering which he obtained from the University of Tennessee at Knoxville in May 2016. He then chose to accept a graduate research assistantship at the University of Tennessee under Dr. James Coder to pursue a Master of Science degree which he completed in August 2018.